Cold-neutron interferometry using beam splitting etalons

KITAGUCHI Masaaki

Errata for KITAGUCHI's doctor thesis

Page 2, section 1.1, Table 1.2

Change nuclear potential value of Co "1180" to "58.7",
change nuclear potential value of Fe "623" to "211".

Cold-neutron interferometry using beam splitting etalons

KITAGUCHI Masaaki

Cold-neutron interferometry using beam splitting etalons

KITAGUCHI Masaaki

Doctor thesis

Department of Physics, Kyoto University

Abstract

Cold-neutron interferometer based on a pair of new devices named 'beam splitting etalons (BSE)' has been developed. The parallelism between the two planes in each BSE and the equality of gap thicknesses of the two BSEs ensure the alignment of four independent multilayer mirrors in the interferometer within the precision required by the three-dimensional coherency of the beam. Flexibility in the arrangements of BSEs enables us to build new types of coherent optical systems for cold neutrons.

The experiment was performed using the cold neutron beam line 'MINE2' at the JRR-3M reactor in JAERI. We have utilized etalons in order to enlarge the spatial separation between two waves in neutron spin interferometer. The present interferometer contains a pair of BSEs. By depositing neutron multilayer mirrors on the parallel planes of an etalon, such an etalon divides the incident neutrons into two parallel paths. The two paths are recombined spatially after the reflection off the second BSE. Using BSEs with an air gap of $9.75\,\mu$m in spacing we have observed interference fringes with the contrast of 60%. The beam had a wavelength of 0.88 nm and a bandwidth of 2.7% in FWHM. The multilayer mirrors had an effective lattice constant of 24 nm. Incident angle for the BSEs through the substrates was 1.05 degree at the wavelength of 0.88 nm. In the viewpoint of geometrical optics, the pair of BSEs is equivalent to a Jamin interferometer, which is the oldest type of interferometer of visible light.

It has been demonstrated that the present etalon plates have sufficient flatness and roughness as substrates for neutron mirrors to compose an interferometer, which require a minimal distortion of wave front. Arranging such mirrors, now we are capable of establishing even a Mach-Zehnder type interferometer. We discuss possible applications for studying fundamental physics. Precision measurement of the topological Aharonov-Casher (AC) effect can be performed by using the present type of interferometer. New type of neutron spin echo spectrometer can be also realized by arranging four BSEs.

Fundamental physics becomes more exciting.

Outline

Chapter 1 introduces optics and interferometry for cold neutrons; reflection off multilayer mirrors and several types of conventional interferometer. Cold neutron interferometer using multilayer mirrors is compared with silicon crystal interferometer for thermal neutrons in this section. In chapter 2 the requirements to construct interferometer for cold neutrons are discussed. The characters of neutron spin interferometer are presented. New type of neutron optical component, called "beam splitting etalon (BSE)," is shown in chapter 3. The BSE is key object in this thesis. Jamin-type interferometer using a pair of BSEs is also proposed in this chapter. All of experiments shown in this thesis were performed at the beam line described in chapter 4. Multilayer fabrication system to deposit neutron mirrors is also described. Jamin-type interferometer using BSEs is demonstrated in chapter 5. Observed interference fringes are shown here. Phase-shift of the interferogram and coherence measurements give clear understanding of the optical system. Discussion about the results is expanded in chapter 6. The wide applicability of the new interferometry using BSEs is discussed in chapter 7. Finally the conclusion of this thesis is presented in chapter 8.

Contents

Chapter 1

Introduction

This chapter introduces basics of neutron optics and interferometry. Neutron interferometry is a powerful technique for studying fundamental physics. A large dimensional interferometer for long wavelength neutrons has the advantage to increase the sensitivity to small interactions. Neutron multilayer mirror, which reflects low energy neutrons according to Bragg's law, is one of the most useful devices in cold neutron optics. Interferometer using multilayer mirrors was realized, however, the small separation between the two paths of the interferometer was one of weak points for applications.

1.1 Multilayer neutron mirror

Slow neutron acts as a matter wave, called as 'de Broglie wave,' which presents various optical phenomena. E. Fermi *et al.* demonstrated the total reflection of neutron wave and defined the refractive index of materials for slow neutrons by using scattering cross section and density of atoms [1]. Through many studies on refraction and diffraction of neutron wave, for example, shown in references [2, 3] and summarized recent works in reference [4], neutron optical devices such as multilayer mirrors and polarizers are utilized for various fields of science.

Reflection and refraction occur when a neutron wave come into a surface. The effective potential V and the refractive index of a material n for slow neutrons is written as

$$V = \frac{2\pi\hbar^2}{m}\nu b, \tag{1.1}$$

$$n \equiv \frac{k'}{k} = \sqrt{1 - \frac{V}{K}} = \sqrt{1 - \frac{\nu b}{\pi}\lambda_n{}^2}, \tag{1.2}$$

where λ_n is neutron wavelength, k is $2\pi/\lambda_n$, m is neutron mass, K is $(\hbar k)^2/2m$, b is neutron scattering length of the nucleus, and ν is the average number density [1, 4]. The index depends on λ_n. The index of most materials is less than 1 and $|1 - n| \sim 10^{-4}$ at $\lambda_n \simeq 10$Å. Table 1.1 shows the potentials of some materials.
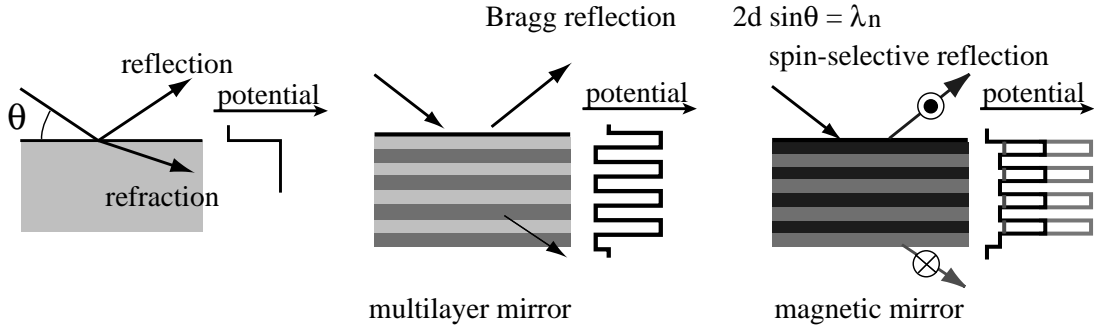
Figure 1.1: Neutron mirrors.

Material	Ni	^{58}Ni	Ti	Ge	V	Si	Al	SiO$_2$
Scattering length [fm]	10.3	14.4	−3.36	8.19	−0.41	4.15	3.45	15.8
Potential [neV]	243.4	340.4	−50.0	94.1	−7.5	54.0	54.1	90.9

Table 1.1: Scattering lengths and potentials of some materials.

Material	Ni	^{58}Ni	Co	Fe	Permalloy45
Nuclear potential [neV]	243.4	340.4	1180	623	220
Magnetic potential [neV]	38.6	38.6	108	132	96.5

Table 1.2: Nuclear and magnetic potentials.

Neutron multilayer mirror is one of the most useful devices in cold neutron optics. Multilayer of two materials with different potentials is understood as a one-dimensional crystal, and such multilayer is suitable for Bragg reflection of long wavelength neutrons (figure 1.1).

A magnetic mirror, in which one of the two materials is ferromagnetic, works as a reflective mirror or as a transparent mirror depending on the polarization of the neutrons. The potential of magnetized material $V_\pm$ for parallel-spin (+) and anti-parallel-spin (−) neutron are

$$V_\pm = V_{\mathrm{nucl}} \pm \mu B, \tag{1.3}$$

where V_{nucl} is the potential which appeared in equation (1.1) and μB is from magnetic interaction. Magnetic potentials of some materials are shown in table 1.2. Multilayer of Permalloy45 (Ni$_{45}$Fe$_{55}$) and germanium has large contrast between the potentials for parallel-spin neutrons and small contrast between the potentials between anti-parallel-spin neutrons. Such multilayer is utilized as a neutron polarizer and an analyzer. The polarization of reflection beam reaches to 95% .

Multilayer is usually made by vacuum evaporation. Ion beam spatter and magnetic

plasma spatter system for fabrication of multilayer are also developed today.

Calculation method for reflectivity of multilayer mirror

The reflectivity of multilayer mirrors can be calculated by numerical method [7]. When a neutron wave with wavenumber of k comes to a surface with the incident angle of θ, the vertical refractive index n_j for the jth layer with the potential of V_j is defined as

$$k_x{}^2 - \frac{2mV_j}{\hbar^2} = n_j{}^2 k^2 = k_j{}^2, \tag{1.4}$$

where the vertical wavenumber $k_x = k\sin\theta$ of the incident wave and k_j is the vertical wavenumber in the jth layer. Schrödinger equation for the vertical wave is

$$\frac{d^2\Psi_j(\zeta)}{d\zeta^2} + n_j\Psi_j(\zeta) = 0, \tag{1.5}$$

where $\zeta = k_j x$. When we define the wave function $\Psi_j(0)$ and its differential $\Psi'_j(0)$ at $\zeta = 0$, we find

$$\begin{pmatrix} \Psi_j(\zeta) \\ \Psi'_j(\zeta) \end{pmatrix} = \begin{pmatrix} \cos n_j\zeta & n_j{}^{-1}\sin n_j\zeta \\ -n_j\sin n_j\zeta & \cos n_j\zeta \end{pmatrix} \begin{pmatrix} \Psi_j(0) \\ \Psi'_j(0) \end{pmatrix}. \tag{1.6}$$

When we define that d_j is the thickness of the jth layer and $\delta_j = k_j d_j$, we find

$$\begin{pmatrix} \Psi_j(\delta_j) \\ \Psi'_j(\delta_j) \end{pmatrix} = \begin{pmatrix} \cos n_j\delta_j & n_j{}^{-1}\sin n_j\delta_j \\ -n_j\sin n_j\delta_j & \cos n_j\delta_j \end{pmatrix} \begin{pmatrix} \Psi_j(0) \\ \Psi'_j(0) \end{pmatrix}. \tag{1.7}$$

The boundary between the jth layer and the $j + 1$th layer is reset to the origin of the depth, therefore,

$$\begin{pmatrix} \Psi_{j+1}(0) \\ \Psi'_{j+1}(0) \end{pmatrix} = M_j \begin{pmatrix} \Psi_j(0) \\ \Psi'_j(0) \end{pmatrix} \tag{1.8}$$

$$M_j = \begin{pmatrix} \cos n_j\delta_j & n_j{}^{-1}\sin n_j\delta_j \\ -n_j\sin n_j\delta_j & \cos n_j\delta_j \end{pmatrix}. \tag{1.9}$$

For multilayer with N layers we can describe

$$\begin{pmatrix} \Psi_{N+1}(0) \\ \Psi'_{N+1}(0) \end{pmatrix} = \begin{pmatrix} A & B \\ C & D \end{pmatrix} \begin{pmatrix} \Psi_1(0) \\ \Psi'_1(0) \end{pmatrix}, \tag{1.10}$$

$$\begin{pmatrix} A & B \\ C & D \end{pmatrix} = M_N \cdots M_2 M_1. \tag{1.11}$$

When the amplitude of incident wave is 1, the reflection amplitude R the transmission amplitude T are obtained as follows

$$\begin{pmatrix} T \\ in_g T \end{pmatrix} = \begin{pmatrix} A & B \\ C & D \end{pmatrix} \begin{pmatrix} 1 + R \\ in_0(1 - R) \end{pmatrix}, \tag{1.12}$$
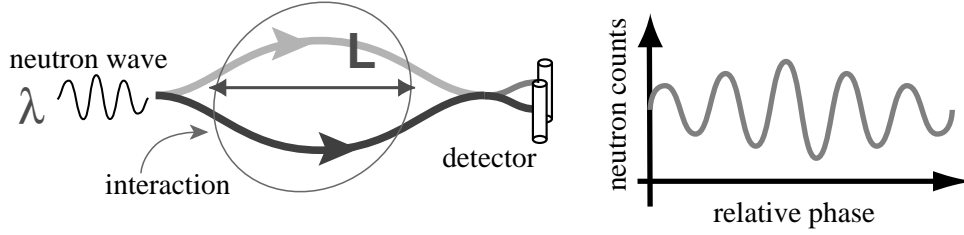
Figure 1.2: Concept of a neutron interferometer.

where n_0 and n_g are the refraction indices of backward and forward side of the multilayer. The reflectivity and the transmittance of the multilayer are described as $|R|^2$ and $|T|^2 n_g/n0$ respectively.

The loss of the potentials of materials which was made by vacuum evaporation was reported [7, 8]. Some advanced methods which consider surface roughness and the loss of the potentials are adopted to correct the calculations[9, 10].

1.2 Neutron interferometer

Neutron interferometry is a powerful technique for studying fundamental physics. Numerous interesting experiments performed in 1970's are reviewed in the reference [5].

Generally an interferometer consists of two paths (figure 1.2). Interference fringes are given as a function of the relative phase. Neutron is a nucleon which has mass, spin, and magnetic moment. Therefore, in neutron interferometry, the relative phase is provided by nuclear, gravitational, spin dependent, and magnetic interaction, or by new physics. We can measure such interactions and search for speculative interactions from the phase of interference fringes. The relative phase $\Delta\phi$ provided by energy difference ΔE between the two beams is written as

$$\Delta\phi = 2\pi \frac{m\lambda_n L}{h^2} \Delta E, \tag{1.13}$$

where L is interaction path length and h is Planck constant. A large dimensional interferometer for long wavelength neutrons has the advantage to increase the sensitivity to small interactions ΔE.

1.2.1 Conventional neutron interferometers

The first success of neutron interferometer was made by using a perfect single crystal, which had been used in X-ray interferometer [11] (figure 1.3). By using a silicon perfect single crystal, H. Rauch *et al.* demonstrated the feasibility of neutron interferometer [12]. Since then, numerous interesting experiments have been performed, for example, measurement of a gravitationally-induced quantum interference [13, 14], Aharonov-Casher effect [15, 16], 4π symmetry of neutron spinor [17, 18], and coherence length of a neutron beam [19, 20].
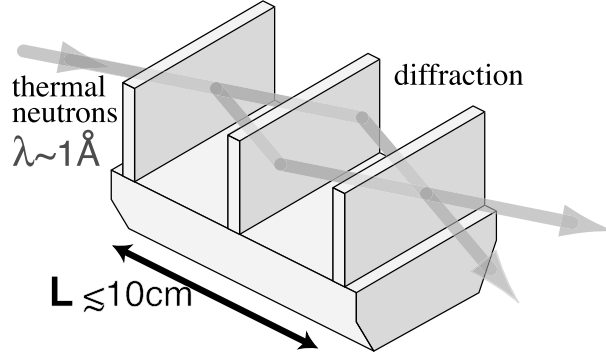
Figure 1.3: Perfect single crystal interferometer

The single-crystal interferometer is inherently not able to deal with a neutron that has a wavelength longer than twice its lattice constant. In order to investigate problems of fundamental physics, the interferometry of cold neutrons is extremely important, since the sensitivity of interferometer for small interaction increases with the neutron wavelength. Large scale of the interaction length is also important, however, the length is limited by size of the crystal. In addition, the dynamical diffraction phenomena require a rather advanced analysis.

Several attempts were made to develop neutron interferometers for cold neutrons and very cold neutrons. Though very cold neutron interferometer using diffraction gratings was demonstrated[21, 22], the separation between the two paths in the interferometer was too small for applications because the lattice constant of the gratings was much larger than the neutron wavelength. Lattice constant of the grating of 2μm and wavelength of 100Å give the opening angle of less than only 0.3 degree.

1.2.2 Cold neutron interferometer using multilayer mirrors

An interferometer with precision alignment of multilayer mirrors enables us to realize the large scale and to utilize long wavelength neutrons. The cold neutron interferometer using multilayer mirrors was demonstrated by H. Funahashi *et al.* [23] . The multilayer interferometer consisted of two "pairmirrors" (figure 1.4). A pairmirror was fabricated by successive vacuum evaporations of multilayer mirror, gap layer, and multilayer mirror. A pairmirror divided incident neutrons into two parallel paths and the relative phase between the two paths of

$$\phi_{\mathrm{PM}} = 2\pi \frac{2D \sin \theta_1}{\lambda_n}, \tag{1.14}$$

was provided. Here D was effective distance between two mirrors and θ_1 was the glancing incident angle of neutron beam. After reflection off the second pairmirror, the two paths were recombined. The relative phase between the two paths was provided by the relative
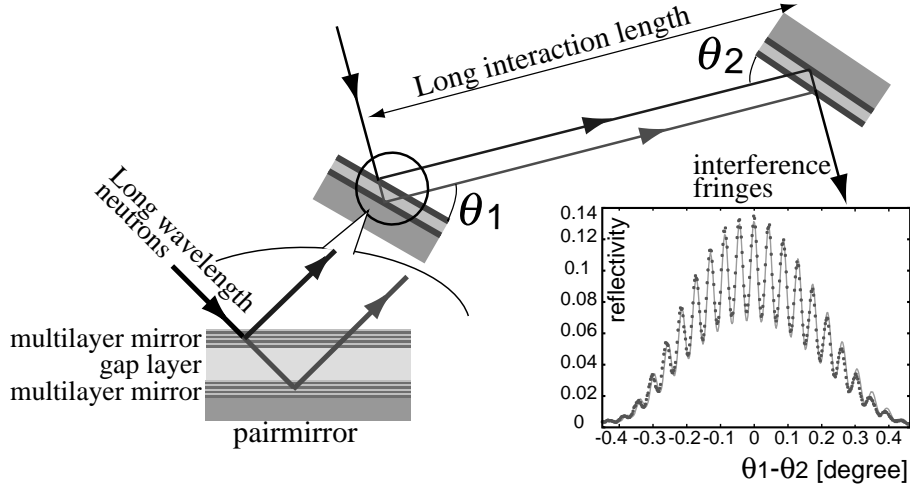
Figure 1.4: Cold-neutron interferometer using multilayer mirrors.

angle between the two pairmirrors,

$$\Delta\phi = 2\pi \frac{2D(\sin\theta_2 - \sin\theta_1)}{\lambda_n}, \tag{1.15}$$

where θ_2 was the incident angle for the second pairmirror. Multiple reflections by the two mirrors in one pairmirror decreased the contrast of observed interferogram. The reflectivity of each mirror was low because of reduction of the multiple reflections, therefore, the intensity after double reflection of two pairmirrors was 10% of the incident beam. The contrast of interference fringes was still about 30% . The parallelism between the two mirrors in each pairmirrors and the equality of gap thicknesses of the two pairmirrors ensured the superposition of the two paths within the precision required by coherency.

The interference fringes by this interferometer is equivalent to 'Brewster fringes' in classical optics. This type of interferometer demonstrated the feasibility of cold neutron interferometer using multilayer mirrors for the first time.

1.2.3   Neutron spin interferometer

Another kind of interferometer using magnetic mirrors was developed, which is based on neutron spin echo method. "Neutron spin interferometer" enables us to carry out high precision experiments due to its high contrast [24].

Neutron spin interferometer using weak magnetic field and radio frequency flippers (RF flippers) was studied by D. Yamazaki *et al.* precisely [25]. A short sketch of the spin interferometer is given here. Vertical magnetic field called as "guiding field" is produced to define the quantized axis and to keep polarity of incident neutrons. The frequency of the oscillating field of RF flipper ω_{RF} is given by

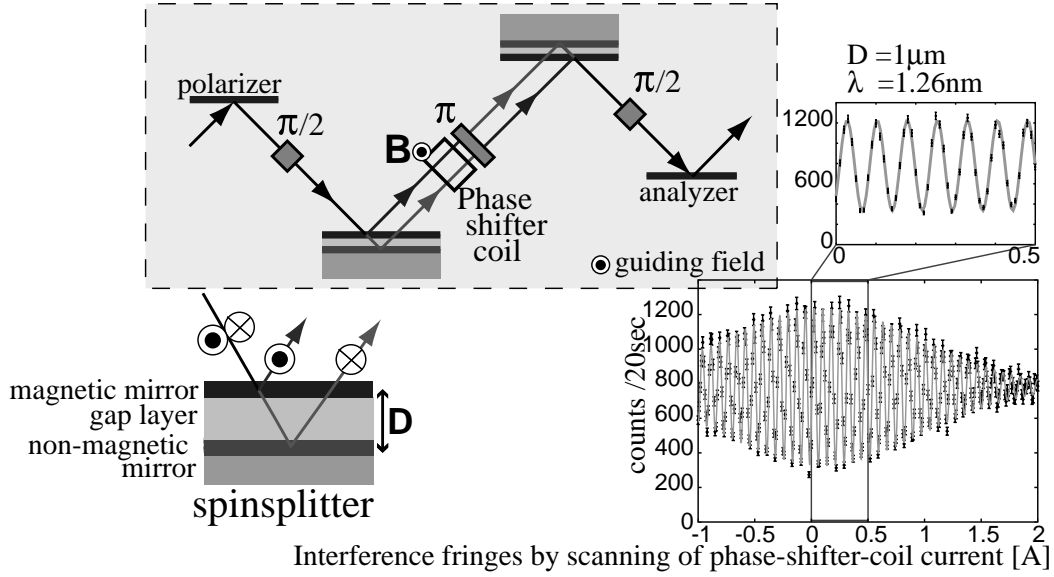$$\hbar\omega_{\mathrm{RF}} = 2\mu B_g, \tag{1.16}$$

Figure 1.5: Neutron spin interferometer with two spinsplitters.

where B_g is the guiding field. The amplitude of the the oscillating field of the RF flipper B_{RF} for $\pi/2$ turn and π turn of neutron spin are given respectively by

$$\frac{\ell}{v}(\mu B_{RF}) = \frac{\pi\hbar}{2}, \tag{1.17}$$

$$\frac{\ell}{v}(\mu B_{RF}) = \pi\hbar, \tag{1.18}$$

where ℓ is the length of the flipper along the neutron beam and v is the neutron velocity. A polarizer makes a beam which is polarized along the guiding field and a $\pi/2$ RF flipper turns the polarity into a direction in the horizontal plane. This action is equivalent to split the incident wave into two coherent waves corresponding to up- and down-spin eigenstates. The polarizer and the $\pi/2$ flipper act as a splitter of an polarization interferometer,

$$| \uparrow > \quad \rightarrow \quad \frac{1}{\sqrt{2}}(| \uparrow > + e^{i\pi/2} | \downarrow >). \tag{1.19}$$

The relative phase of $\pi/2$ between the spin-flipped component and non-flipped component is provided through the RF flipper. The relative phase between the two components is also provided by phase-shifter coil as

$$\phi_C = \gamma H t, \tag{1.20}$$

where γ is the gyromagnetic ratio of neutron, H is magnetic field of phase-shifter coil, t is time of flight through the coil. Hence,

$$\frac{1}{\sqrt{2}}(| \uparrow > + e^{i\pi/2} | \downarrow >) \quad \rightarrow \quad \frac{1}{\sqrt{2}}(| \uparrow > + e^{i\phi_C} e^{i\pi/2} | \downarrow >). \tag{1.21}$$

The relative phase $e^{i\phi_C}$ is marked up to $|\downarrow>$. Usually the two spin of each component is flipped by π flipper in order to decrease effects of external magnetic field noise,

$$\frac{1}{\sqrt{2}}(|\uparrow> + e^{i\phi_C}e^{i\pi/2}|\downarrow>) \quad \rightarrow \quad \frac{1}{\sqrt{2}}(|\downarrow> + e^{i\phi_C}e^{i\pi/2}|\uparrow>), \tag{1.22}$$

where the phase added by π flipper to both of the two components is omitted. The second $\pi/2$ RF flipper split the each component into two spin eigenstates again,

$$\frac{1}{\sqrt{2}}e^{i\phi_C}e^{i\pi/2}|\uparrow> \quad \rightarrow \quad \frac{1}{2}e^{i\phi_C}(e^{i\pi/2}|\uparrow> + e^{i\pi}|\downarrow>), \text{and} \tag{1.23}$$

$$\frac{1}{\sqrt{2}}|\downarrow> \quad \rightarrow \quad \frac{1}{2}(e^{i\pi/2}|\uparrow> + |\downarrow>). \tag{1.24}$$

After spin analyze, up-spin components from the two components are superposed and the relative phase ϕ_C can be observed as neutron counts,

$$\text{Reflection off Analyzer} \quad \rightarrow \quad \frac{1}{2}e^{i\pi/2}(|\uparrow> + e^{i\phi_C}|\uparrow>) \tag{1.25}$$

$$\text{Transmission through Analyzer} \quad \rightarrow \quad \frac{1}{2}(|\downarrow> + e^{i\phi_C}e^{i\pi}|\downarrow>). \tag{1.26}$$

We detect neutron counts which change according to

$$\left|\frac{1}{2}(|\uparrow> + e^{i\phi_C}|\uparrow>)\right|^2 = \frac{1}{2}(1 + \cos\phi_C). \tag{1.27}$$

In order to split the two spin components into two spatial paths, a pair of neutron devices called as 'spinsplitters' was inserted in the interferometry (figure 1.5) [24]. A spinsplitter consisted of magnetic mirror on top, gap layer, and non-magnetic mirror. The magnetic mirror reflected only the spin-up component and a non-magnetic neutron mirror reflected the spin-down component which was transmitted through the magnetic mirror. The spinsplitter provided relative phase of

$$\phi_{SS} = 2\pi \frac{2D\sin\theta}{\lambda_n}, \tag{1.28}$$

where D was effective distance between two mirrors and θ was the glancing incident angle of neutron beam. The two waves were superposed each other spatially on the second spinsplitter. We were able to provide the relative phase not only the relative angle between the spinsplitters but also the magnetic field of phase-shifter coil. Though figure 1.5 shows one of examples of interference fringes, high contrast of about 70% was reported. High intensity due to high reflectivity of the mirrors in spinsplitters also has the advantage to perform experiments.

There were some remarkable experiments using the other type of interferometer with magnetic mirrors, for example, double Stern-Gerlach experiments [26] and delayed choice experiments [27].
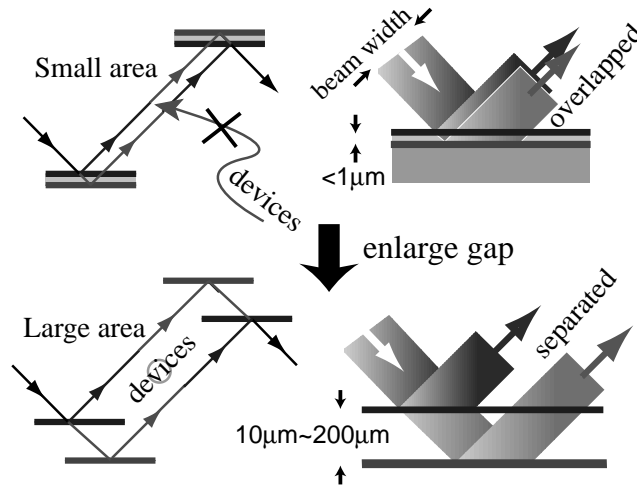
Figure 1.6: Advantage of large gaps.

1.3 Development of large-scale interferometer

The range of application of the cold-neutron interferometer using multilayer mirrors is limited due to the small spatial separation between two beams (figure 1.6). Because the gap layer of a conventional pairmirror or spinsplitter is fabricated with vacuum evaporation method, the gap is not thick enough to separate the two beams spatially, on the order of 1μm.

A cold neutron interferometer with large spatial separation enables us to carry out much higher precision measurements and new types of experiment. With the large separation we can insert some devices into the gap between paths of the interferometer, for example, to investigate the topological nature of AC effect [16]. The aim of the study described in this thesis is to increase the spatial beam separation of a multilayer interferometer in order to broaden the applicability of neutron interferometry.

Chapter 2

Interference

Requirements to observe interference fringes in neutron interferometer are presented. Coherency of the beam is determined by beam properties of monochromaticity and collimation. "Shiftless component", which prevents us from finding phase-shift to be searched for, is introduced in this chapter. General aspect of dispersion relation for phase-shifters is mentioned.

2.1 Two beam interference

Coherency between two waves is generally presented by using space-time correlation function between the waves [6]. Here we treat only Gaussian wave in order to give clear understanding by following the discussion presented in reference [28]. Wave function Ψ^{inc} has a wave number of k, which has mean of k_0 and a standard deviation of $\sqrt{2}\,\sigma_k$.

$$\Psi^{\text{inc}} = \frac{1}{\sqrt{2\pi}} \int g(k) e^{i(kx - \omega t)} dk \quad , \quad g(k) \equiv \frac{1}{(2\pi\sigma_k{}^2)^{1/4}} \exp\{-\frac{(k - k_0)^2}{2(\sqrt{2}\,\sigma_k)^2}\}, \tag{2.1}$$

where m is mass of neutron and $\hbar\omega \equiv \frac{(\hbar k)^2}{2m}$. $|g(k)|^2$ has Gaussian distribution having a mean of k_0 and a standard deviation of σ_k. Here a factor for normalization of $1/(2\pi\sigma_k{}^2)^{1/4}$ is described as N below.

The wave is divided into ψ^{I} and ψ^{II} by a splitter. The relative phase between the two waves is written as $\phi(k, \xi)$, where ξ is a parameter of a phase shifter. The relative phase is expanded to

$$\phi(k, \xi) \approx \phi_0(\xi) + L_0(\xi)(k - k_0), \tag{2.2}$$

and here define ϕ_0 and $L_0(\xi)$.

$$\phi_0(\xi) \equiv \phi(k_0, \xi) \ , \ \ L_0(\xi) \equiv \left. \frac{\partial \phi(k, \xi)}{\partial k} \right|_{k=k_0}. \tag{2.3}$$

ψ^{I} and ψ^{II} are described by using the real number a_{I} and a_{II} as

$$
\begin{aligned}
\psi^{\mathrm{I}} &= \frac{a_{\mathrm{I}}}{\sqrt{2\pi}} \int g(k) e^{kx-\omega t} dk & (2.4) \\
&= \frac{a_{\mathrm{I}} N}{\sqrt{(\sqrt{2}\,\sigma_k)^{-2} + i\frac{\hbar}{m}t}} \exp\left\{ -\frac{(x - \frac{\hbar k_0}{m}t)^2}{2((\sqrt{2}\,\sigma_k)^{-2} + i\frac{\hbar}{m}t)} \right\} e^{i(k_0 x - \omega_0 t)} & (2.5) \\
\psi^{\mathrm{II}} &= \frac{a_{\mathrm{II}}}{\sqrt{2\pi}} \int g(k) e^{kx-\omega t} e^{\phi(k,\xi)} dk & (2.6) \\
&= \frac{a_{\mathrm{II}} N}{\sqrt{(\sqrt{2}\,\sigma_k)^{-2} + i\frac{\hbar}{m}t}} \exp\left\{ -\frac{((x + L_0(\xi)) - \frac{\hbar k_0}{m}t)^2}{2((\sqrt{2}\,\sigma_k)^{-2} + i\frac{\hbar}{m}t)} \right\} e^{i(k_0 x - \omega_0 t)} e^{i\phi_0(\xi)} & (2.7)
\end{aligned}
$$

where $\hbar\omega_0 \equiv \frac{(\hbar k_0)^2}{2m}$. When we don't consider absorption in the splitter, then $a_{\mathrm{I}}{}^2 + a_{\mathrm{II}}{}^2 = 1$, where $a_{\mathrm{I}}{}^2$ and $a_{\mathrm{II}}{}^2$ are correspond to reflectivity and transmittance of the splitter respectively. We find

$$
\begin{aligned}
|\psi^{\mathrm{I}}|^2 &= \frac{|a_{\mathrm{I}}|^2}{\sqrt{2\pi((\sigma_{x0})^2 + (\sigma_v t)^2)}} \exp\left\{ -\frac{(x - v_g t)^2}{2((\sigma_{x0})^2 + (\sigma_v t)^2)} \right\} & (2.8) \\
|\psi^{\mathrm{II}}|^2 &= \frac{|a_{\mathrm{II}}|^2}{\sqrt{2\pi((\sigma_{x0})^2 + (\sigma_v t)^2)}} \exp\left\{ -\frac{((x + L_0(\xi)) - v_g t)^2}{2((\sigma_{x0})^2 + (\sigma_v t)^2)} \right\} & (2.9)
\end{aligned}
$$

$$
\sqrt{2}\,\sigma_{x0} \equiv \frac{1}{\sqrt{2}\,\sigma_k} \;,\; v_g \equiv \frac{\hbar k_0}{m} \;,\; \sigma_v \equiv \frac{\hbar}{m}\sigma_k, \qquad (2.10)
$$

where $\sqrt{2}\sigma_{x0}$ is the standard deviation of Fourier transformation of $g(k)$, v_g is the velocity of center of wave packet, and σ_v is the standard deviation of the velocity distribution. From equation (2.8) and (2.9) we can understand that there is a spatial shift of $L_0(\xi)$ between the center of the wave packets of ψ^{I} and ψ^{II}. $L_0(\xi)$ can be regarded as the optical-path difference between the two paths.

After superposition by an analyzer, the wave function and the intensity are written as

$$
\begin{aligned}
\Psi^{\mathrm{sup}} &= \frac{N}{\sqrt{(\sqrt{2}\,\sigma_{x0}) + i\frac{\hbar}{m}t}} e^{i(k_0 x - \omega t)} \times \left\{ a_{\mathrm{I}}' \exp\left\{ -\frac{(x - v_g t)^2}{2((\sqrt{2}\,\sigma_{x0})^2 + i\frac{\hbar}{m}t)} \right\} \right. \\
&\quad \left. + a_{\mathrm{II}}' e^{i\phi_0(\xi)} \exp\left\{ -\frac{((x + L_0(\xi)) - v_g t)^2}{2((\sqrt{2}\sigma_{x0})^2 + i\frac{\hbar}{m}t)} \right\} \right\}, & (2.11)
\end{aligned}
$$

$$
\begin{aligned}
I(\xi) &= \int |\Psi^{\mathrm{sup}}|^2 dx \\
&= (a_{\mathrm{I}}'^2 + a_{\mathrm{II}}'^2) + 2a_{\mathrm{I}}' a_{\mathrm{II}}' \exp\left\{ -\frac{1}{2}(\sigma_k L_0(\xi))^2 \right\} \cos(\phi_0(\xi)), & (2.12)
\end{aligned}
$$

where a_{I}' and a_{II}' are amplitudes of the two paths after the analyzer and $\lambda_0 = 2\pi/k_0$. When changes of a_{I}' and a_{II}' are small by ξ scan, the intensity in equation (2.12) means interference fringes according to $\cos(\phi_0(\xi))$.

Phase of interference fringes $\phi_0(\xi)$ depends only on k_0 and ξ, and doesn't depend on σ_k. Distribution of wavenumber does not affect the phase of interferogram. σ_k and $L_0(\xi)$ define the amplitude of interference fringes and affect the contrast of the fringes. The contrast of interference fringes $\Upsilon(\sigma_k, \xi)$ is written by using ξ and σ_k

$$\Upsilon(\sigma_k, \xi) \quad = \quad \frac{2a_\mathrm{I}{}' a_\mathrm{II}{}'}{a_\mathrm{I}{}'^2 + a_\mathrm{II}{}'^2} \, \Gamma(\sigma_k, L_0(\xi)) \tag{2.13}$$

$$\Gamma(\sigma_k, L_0(\xi)) \quad \equiv \quad \exp\left\{ -\frac{1}{2} \left(\sigma_k L_0(\xi) \right)^2 \right\} \tag{2.14}$$

We obtain that the contrast of interference fringes $\Upsilon(\sigma_k, \xi)$ is proportional to the coherence function $\Gamma(\sigma_k, L_0(\xi))$. The value of $\Gamma(\sigma_k, L_0(\xi))$ decreases monotonously with σ_k and $L_0(\xi)$. At $L_0(\xi) = 0$, the contrast becomes maximum. The maximum contrast point is called as "echo point." Coherence length L^c is usually defined as the optical path-difference which gives the contrast of $1/e$ of the maximum. We obtain

$$\sigma_k L^c = \sqrt{2}. \tag{2.15}$$

Optical components in an interferometer must be arranged within the precision which don't make the optical path-difference as large as twice of the coherence length to observe clear interference fringes. This leads the requirements for design of the components and precision of arrangement. In the case of cold neutron beam line which is used for our experiments described in this thesis (see section 4.2), k_0 is $7.14\,\mathrm{nm}^{-1}$ and σ_k is $0.083\,\mathrm{nm}^{-1}$, therefore, the coherence length L^c is $17\,\mathrm{nm}$.

The transverse coherency can be discussed as the longitudinal case presented above,

$$\sigma_{k\perp} L_\perp{}^c = \sqrt{2}. \tag{2.16}$$

The standard deviation of the transverse wavenumber is determined by the collimation of the beam. The typical value of $\sigma_{k\perp}$ for horizontal direction and vertical direction are $0.00095\,\mathrm{nm}^{-1}$ and $0.030\,\mathrm{nm}^{-1}$ respectively. The coherence length for horizontal direction and vertical direction are $1.5\,\mu\mathrm{m}$ and $47\,\mathrm{nm}$ respectively. The transverse coherence lengths can be changed by changing of the beam collimation.

2.2   Shiftless component in neutron spin interferometer

In neutron spin interferometry incident wave is divided into spin components and spatial paths. The relative phase is provided not only by the relative angle between the spinsplitters but also by the magnetic field of phase-shifter coil.

When one spatial path contains both of up- and down-spin components, the magnetic field provides the relative phase between the two components. The interference fringes which are oscillated by the relative phase between the two spin components in one spatial path don't shift through the change of the optical path-difference between the two spatial paths. We call this component as "shiftless component" in this thesis. Shiftless component is noise for measurements of the phase-shift according to the energy difference between two spatial paths.
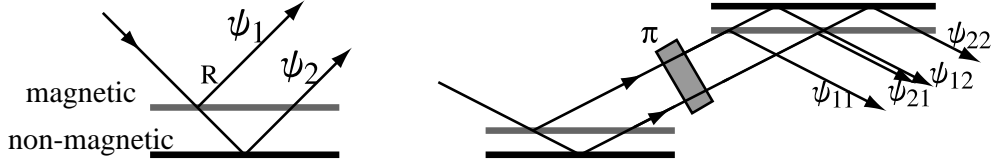
Figure 2.1: Spatial paths with spinsplitters. (Left) Two paths from one spinsplitter. (Right) Four paths from two spinsplitters.

Because the fringes from the shiftless component mixes with the fringes from the two spatial paths in scanning of the spin interferometer with two spinsplitters, we cannot measure only the shiftless component directly in the interferometer. However, the shiftless component can be measured by the interferometer with one spinsplitter. When the gap thickness D is sufficiently large, the optical path-difference of $2D\sin\theta$ between two spatial paths, which is made by reflection off the spinsplitter with the incident angle of θ, is too larger than the coherence length. The contrast of the interference fringes by the relative phase between the spatial paths decreases to zero. On the other hand, the contrast of the fringes by the shiftless component retains visible level. Here we consider that the reflectivity of the magnetic mirror of spinsplitters is not perfect. For simple discussion we assume that the reflectivity of non-magnetic mirror is perfect and that absorption in all mirrors is ignored. The performance of mirrors for our experiments, which are described in section 5.1, is good enough to accept this. We consider the incident beam of $\frac{1}{\sqrt{2}}(|\uparrow> + |\downarrow>)$. The phases added by RF flippers are omitted below. The spatial path reflected by the magnetic mirror ψ_1 and the path reflected by the non-magnetic mirror ψ_2 are written as

$$\psi_1 \;=\; \frac{1}{\sqrt{2}}(R_\uparrow\,|\uparrow> + R_\downarrow\,|\downarrow>) \tag{2.17}$$

$$\psi_2 \;=\; \frac{1}{\sqrt{2}}e^{i\phi_{\mathrm{SS}}}(T_\uparrow T_\uparrow\,|\uparrow> + T_\downarrow T_\downarrow|\downarrow>), \quad \phi_{\mathrm{SS}} = 2\pi 2D\sin\theta/\lambda_n, \tag{2.18}$$

where R and T is the reflection amplitude and the transmission amplitude of the magnetic mirror for up- and down-spin neutrons (figure 2.1). After the relative phase ϕ_{C} is provided by the phase-shifter coil, neutrons are counted through the analyzer. The optical path-difference between ψ_1 and ψ_2 is $2D\sin\theta$, which is too long to observe interference fringes between the two paths (equation (2.14)), therefore, the intensity I is written as

$$I \;=\; \left|\frac{1}{2}(R_\uparrow\,|\uparrow> + e^{i\phi_{\mathrm{C}}}R_\downarrow\,|\downarrow>)\right|^2 + \left|\frac{1}{2}e^{i\phi_{\mathrm{SS}}}(T_\uparrow T_\uparrow\,|\uparrow> + e^{i\phi_{\mathrm{C}}}\,T_\downarrow T_\downarrow|\downarrow>)\right|^2 \tag{2.19}$$

$$=\; \frac{1}{4}(R_\uparrow{}^2 + R_\downarrow{}^2 + 2R_\uparrow R_\downarrow\cos\phi_{\mathrm{C}}) + \frac{1}{4}(T_\uparrow{}^4 + T_\downarrow{}^4 + 2T_\uparrow{}^2 T_\downarrow{}^2\cos\phi_{\mathrm{C}}). \tag{2.20}$$

The phase of interference fringes does not shift for changing of ϕ_{SS}. The contrast from

the shiftless component is

$$\Upsilon_{\text{OneSS}} = \frac{2(R_\uparrow R_\downarrow + T_\uparrow{}^2 T_\downarrow{}^2)}{R_\uparrow{}^2 + R_\downarrow{}^2 + T_\uparrow{}^4 + T_\downarrow{}^4}. \tag{2.21}$$

When $R_\downarrow^2$ and $T_\uparrow^4$ is small, and $R_\uparrow^2$ and $T_\downarrow^4$ is nearly 1, we find

$$\Upsilon_{\text{OneSS}} \sim R_\uparrow R_\downarrow + T_\uparrow{}^2 T_\downarrow{}^2. \tag{2.22}$$

After the reflection off the second spinsplitter, four paths shown in figure 2.1 are written as

$$\psi_{11} = \frac{1}{\sqrt{2}}(R_\uparrow R_\downarrow \,|\uparrow> + R_\downarrow R_\uparrow \,|\downarrow>) \tag{2.23}$$

$$\psi_{12} = \frac{1}{\sqrt{2}} e^{i\phi_{\text{SS}}} T_\downarrow{}^2 R_\uparrow \,|\downarrow> \tag{2.24}$$

$$\psi_{21} = \frac{1}{\sqrt{2}} e^{i(\phi_{\text{SS}}+\Delta\phi)} R_\uparrow T_\downarrow{}^2 \,|\uparrow> \tag{2.25}$$

$$\psi_{22} = \frac{1}{\sqrt{2}} e^{i(2\phi_{\text{SS}}+\Delta\phi)} (T_\uparrow{}^2 T_\downarrow{}^2 \,|\uparrow> + T_\downarrow{}^2 T_\uparrow{}^2 \,|\downarrow>), \tag{2.26}$$

where $\Delta\phi$ is the relative phase added by the relative angle between the two spinsplitters. The poor components which come along the unfavorable paths at both of reflections off the two spinsplitters are omitted. When the optical path-difference between ψ_{12} and ψ_{21} is small enough to observe interference fringes, the intensity through the phase-shifter coil and the analyzer is

$$\begin{aligned} I &= \left| \frac{1}{2} \left(R_\uparrow R_\downarrow \,|\uparrow> + e^{i\phi_{\text{C}}} R_\uparrow R_\downarrow \,|\uparrow> \right) \right|^2 + \left| \frac{1}{2} \left(T_\uparrow{}^2 T_\downarrow{}^2 \,|\uparrow> + e^{i\phi_{\text{C}}} T_\uparrow{}^2 T_\downarrow{}^2 \,|\uparrow> \right) \right|^2 \\ &\quad + \left| \frac{1}{2} \left(T_\downarrow{}^2 R_\uparrow \,|\uparrow> + e^{i(\phi_{\text{C}}-\Delta\phi)} T_\downarrow{}^2 R_\uparrow \,|\uparrow> \right) \right|^2 \tag{2.27} \\ &= \frac{1}{2} \left((R_\uparrow R_\downarrow)^2 + (R_\uparrow R_\downarrow)^2 \cos\phi_{\text{C}} + (T_\uparrow{}^2 T_\downarrow{}^2)^2 + (T_\uparrow{}^2 T_\downarrow{}^2)^2 \cos\phi_{\text{C}} \right. \\ &\quad \left. + (T_\downarrow{}^2 R_\uparrow)^2 + (T_\downarrow{}^2 R_\uparrow)^2 \cos(\phi_{\text{C}} - \Delta\phi) \right). \tag{2.28} \end{aligned}$$

Only last term depends on $\Delta\phi$ and the optical path-difference between the two spatial paths. The contrast of the interference fringes from the two spatial paths is

$$\Upsilon_{\text{DoubleSS}} = \frac{(T_\downarrow{}^2 R_\uparrow)^2}{(R_\uparrow R_\downarrow)^2 + (T_\uparrow{}^2 T_\downarrow{}^2)^2 + (T_\downarrow{}^2 R_\uparrow)^2}. \tag{2.29}$$

The intensity described as (2.28) contains interference fringes from shiftless component with the contrast of

$$\Upsilon_{\text{Shiftless}} = \frac{(R_\uparrow R_\downarrow)^2 + (T_\uparrow{}^2 T_\downarrow{}^2)^2}{(R_\uparrow R_\downarrow)^2 + (T_\uparrow{}^2 T_\downarrow{}^2)^2 + (T_\downarrow{}^2 R_\uparrow)^2}. \tag{2.30}$$

When $R_\downarrow{}^2$ and $T_\uparrow{}^4$ is small, and $R_\uparrow^2$ and $T_\downarrow^4$ is nearly 1, we obtain

$$
\begin{aligned}
\Upsilon_{\text{Shiftless}} \quad &\sim \quad (R_\uparrow R_\downarrow)^2 + (T_\uparrow{}^2 T_\downarrow{}^2)^2 & (2.31)\\
&\lesssim \quad (\Upsilon_{\text{OneSS}})^2. & (2.32)
\end{aligned}
$$

This means that the contrast of interference fringes from shiftless component with two spinsplitters is less than the square of the contrast of fringes with one spinsplitter.

2.3   Dispersion relation

In neutron spin interferometer, the relative phase between two spatial paths which are characterized by spin eigenstates are provided not only by the relative angle between the spinsplitters but also by the magnetic field of phase-shifter coil. But they are different in momentum dependence.

The relative phase provided by a pair of spinsplitters ϕ_{SS} is expressed with the distance between the two mirrors D, the incident angle of the first spinsplitter θ_1[rad], and that of the second θ_2[rad] as

$$
\begin{aligned}
\phi_{\text{SS}} \quad &= \quad 2\pi \frac{2D(\sin\theta_2 - \sin\theta_1)}{\lambda_n} \\
&\simeq \quad 2D\,\delta\theta\,\frac{2\pi}{\lambda_n} \\
&\equiv \quad A_{\text{SS}}\,\delta\theta\,k, & (2.33)
\end{aligned}
$$

where $\delta\theta$ is the relative angle between the two spinsplitters $(\theta_2 - \theta_1)$. The relative phase provided by phase-shifter coil ϕ_{C} is

$$
\begin{aligned}
\phi_{\text{C}} \quad &= \quad \gamma H t \\
&\equiv \quad A_{\text{C}}\,j\,\frac{1}{k}, & (2.34)
\end{aligned}
$$

where γ is the gyromagnetic ratio of neutron, H is magnetic field of phase-shifter coil, t is time of flight through the coil, which is proportional to k^{-1}, j is the current of phase-shifter-coil, and A_{C} is a conventional constant. The ϕ_{SS} and the ϕ_{C} are different in k dependence. The sum of relative phase between the two paths is

$$
\begin{aligned}
\phi(k, \delta\theta, j) \quad &= \quad \phi_{\text{SS}} + \phi_{\text{C}} \\
&\simeq \quad \{A_{\text{SS}}\,\delta\theta\,k_0 + A_{\text{SS}}\,\delta\theta(k - k_0)\} \\
&\qquad + \{\frac{A_{\text{C}}\,j}{k_0} - \frac{A_{\text{C}}\,j}{k_0{}^2}(k - k_0)\} \\
&= \quad (A_{\text{SS}}\,\delta\theta\,k_0 + \frac{A_{\text{C}}\,j}{k_0}) \\
&\qquad + (A_{\text{SS}}\,\delta\theta - \frac{A_{\text{C}}\,j}{k_0{}^2})(k - k_0). & (2.35)
\end{aligned}
$$

Using the expression of equation (2.2) , we find

$$\phi_0 \quad = \quad A_{\mathrm{SS}}\,\delta\theta k_0 + \frac{A_{\mathrm{C}}}{k_0}\,j \tag{2.36}$$

$$L_0 \quad = \quad A_{\mathrm{SS}}\,\delta\theta - \frac{A_{\mathrm{C}}}{k_0{}^2}\,j. \tag{2.37}$$

Equation (2.36) shows that a period of interferogram by scanning phase-shifter-coil current is $\dfrac{2\pi k_0}{A_{\mathrm{C}}}$ [A] when $\delta\theta$ is fixed, and that a phase of interferogram shifts by $-\dfrac{A_{\mathrm{SS}}k_0}{2\pi}\Delta\theta$ cycles when changing $\delta\theta$ by $\Delta\theta$. On the other hand, equation (2.37) shows that an echo-point shifts by $+\dfrac{A_{\mathrm{SS}}k_0}{2\pi}\Delta\theta$ cycles, which is equal quantity to the reverse direction of the phase-shift of interferogram. To observe this action the reflectivity of multilayer mirrors must be kept through changing of $\Delta\theta$. It is difficult to keep the reflectivity of the multilayer mirrors in the wide range of incident angle, therefore, it is not easy to observe this action clearly by using spinsplitters with small gaps which require large $\Delta\theta$. Spinsplitters with large gaps make $\Delta\theta$ small enough to observe this action clearly, which has a negligible the effect on the mirror reflectivity.

In addition, this means that one of the phase-difference and optical path-difference can be changed independently.

Chapter 3

Beam splitting etalons

A new type of neutron optical component named "beam splitting etalon (BSE)" is proposed. By arranging Jamin-type interferometer with a pair of BSEs, the spatial separation between the two paths in the interferometer can be enlarged.

3.1 Etalons

One of weak points of the conventional cold neutron interferometer using multilayer mirrors is small separation between the two paths in the interferometer. The small separation was caused by thin gap layer of pairmirrors. We have utilized etalons in order to enlarge the gap. An etalon is an optical device, mainly used in laser optics, which has two parallel planes (figure 3.1). In common use, multilayer dielectric mirrors for laser are coated on the two planes and construct Fabry-Perot interferometer with vertical incident laser. Such etalons function as filters which produce sharp transmission peaks. Etalons are classified into two types; air-spaced etalons and solid etalons.

Air-spaced etalon consists of two substrates which have smooth planes individually and the planes face each other with spacers between the two substrates. They are bonded by optical contact method. The parallelism between the two planes depends on the precision of the spacers.

Solid etalon is one substrate which have parallel planes on both sides.
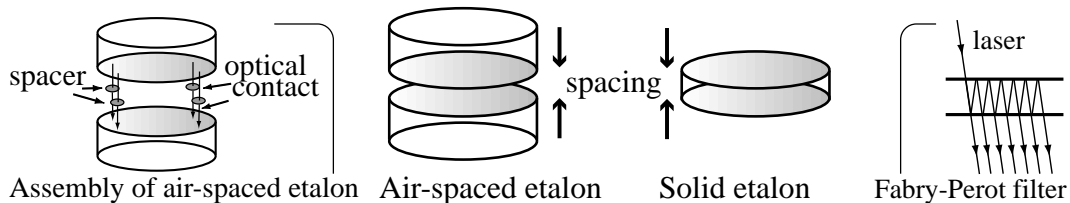
Figure 3.1: Air-spaced etalon and solid etalon.
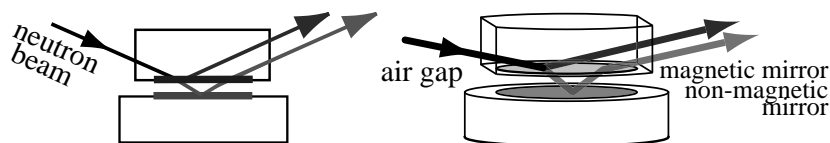
Figure 3.2: Beam splitting etalon.

The substrates of etalons are made of fused silica. The spacers of air-spaced etalons are made with material which have higher thermal stability, like Zerodure. The spacing between the two planes of air-spaced and solid etalon depends on the spacer and the substrate respectively.

3.2   Beam splitting etalons

Multilayer neutron mirrors in a pairmirror or a spinsplitter can be replaced with two mirrors on the two parallel planes of an etalon. The spacing of the etalon is regarded as the gap thickness of the pairmirror. The gap layer of the pairmirror can not be thick because of technical problems of vacuum evaporation. On the other hand, the spacing of an etalon can be enlarged. Surface roughness of etalon substrates for laser optics is not enough smooth to use neutron mirror substrates, however, we can purchase special etalons with planes smooth enough to be used as substrates of neutron mirrors today. We call this type of neutron optical components as "beam splitting etalon (BSE)." Both side of one etalon plate is finished to flat for entrance and exit of neutron beam (figure 3.2).

When a magnetic neutron mirror is deposited on one of planes of BSE and a non-magnetic mirror is deposited on the another plane, the BSE functions as a spinsplitter with the large gap. The magnetic mirror reflects only the spin-up component and a non-magnetic neutron mirror reflects the spin-down component which is transmitted through the magnetic mirror.

3.3   Requirements for Jamin-type arrangement

By using a pair of beam splitting etalons, an interferometer for cold neutrons can be constructed. In the viewpoint of geometrical optics the pair of BSEs is equivalent to a Jamin interferometer, which is the oldest type of interferometer for practical use in the history of optics (figure 3.3). Spatial separation between two paths in cold-neutron multilayer interferometer can be enlarged by using BSEs.

Because the optical path-difference between the two paths is compensated by the reflection off the two BSEs, interference fringes with high contrast can be observed. The effect of the beam divergence can be also canceled in this geometry [23]. The relative
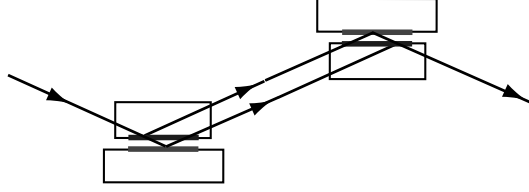
Figure 3.3: Jamin-type arrangement with a pair of BSEs.

phase from the geometry is

$$
\begin{aligned}
\Delta\phi &= 2\pi \frac{2D(\sin\theta_2 - \sin\theta_1)}{\lambda_n} \\
&\simeq 2\pi\, 2D\delta\theta/\lambda_n,
\end{aligned}
\tag{3.1}
$$

where the incident angle to the spacing of the first BSE and the second BSE are θ_1 and θ_2, and D is the effective distance between the two mirrors in the BSE due to the spacing. The incident angle to the BSE is little smaller than θ_1 and θ_2 due to the refraction of the etalon substrate. Neutrons which are reflected by the first BSE with the incident angle of $\theta_1 + \epsilon$ are inputed into the second BSE with the incident angle of $\theta_2 + \epsilon$. The relative phase don't change as

$$
\begin{aligned}
\Delta\phi &= 2\pi \frac{2D(\sin(\theta_2 + \epsilon) - \sin(\theta_1 + \epsilon))}{\lambda_n} \\
&\simeq 2\pi\, 2D\delta\theta/\lambda_n.
\end{aligned}
\tag{3.2}
$$

Here we discuss requirements for assembly and arrangement of the BSEs as the optical path-difference between the superposed two waves is less than coherence length. Requirements for one BSE which have displacements from ideal case are found, when the other BSE is ideal. We consider typically the case that the incident angle to BSEs θ is 1 degree and the spacing of D is $10\,\mu$m. For our experiments at the beam line MINE2 (see section 4.2), the longitudinal coherence length $L_L{}^c$ of $17\,$nm is considered. We suppose appropriately for our experiments that the transverse coherence length for horizontal direction $L_H{}^c$ and for vertical direction $L_V{}^c$ are $1.5\,\mu$m and of $47\,$nm respectively.

3.3.1 Equality of spacing

When there is the difference of spacing between two BSEs ΔD, the longitudinal optical path-difference is $2\Delta D \sin\theta$, then the requirement on ΔD is

$$
2\Delta D \sin\theta \;\lesssim\; L_L{}^c
\tag{3.3}
$$
$$
\Delta D \;\lesssim\; 0.5\,\mu\text{m} \quad (L_L{}^c = 17\,\text{nm}, D = 10\,\mu\text{m}, \theta = 1\,\text{degree}).
\tag{3.4}
$$

At the same time there is the transverse shift of $2\Delta D \cos\theta$ for horizontal direction (figure 3.4 (1)). We obtain

$$
2\Delta D \cos\theta \;\lesssim\; L_H{}^c
\tag{3.5}
$$
$$
\Delta D \;\lesssim\; 0.7\,\mu\text{m} \quad (L_H{}^c = 1.5\,\mu\text{nm}, D = 10\,\mu\text{m}, \theta = 1\,\text{degree}).
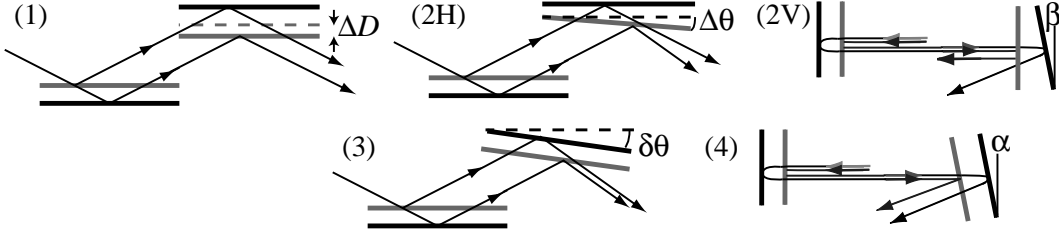\tag{3.6}
$$

Figure 3.4: Displacement of mirrors. (1) Difference of spacing. (2) Wedge angle between mirrors in BSE for horizontal (2H) and vertical direction (2V). (3) Relative angle between two BSEs. (4) Tilting angle of BSE. (1)(2H)(3) are top view, and (2V)(4) are horizontal view tangential to mirror surfaces (see also figure 5.8).

This means that equality within $0.5\,\mu$m for spacing of the BSEs is required to observe clear interference fringes. Today's technique for assembly of etalons, which uses the spacers polished at the same time, can supply such equal etalons with more precision of $\lambda_{\text{He-Ne}}/150$, which is equivalent to $4\,$nm.

3.3.2   Parallelism between two planes

When the one plane in one BSE is at an angle of $\Delta\theta$ to the other plane, the superposed two beams are opened with the angle of $2\Delta\theta$. Assuming that the distance between the etalon and the detector is $\mathcal{L}$, the superposed beams at the detector position have the shift of $2\mathcal{L}\Delta\theta$, then

$$2\mathcal{L}\Delta\theta \;\lesssim\; L_H{}^c \tag{3.7}$$

$$\Delta\theta \;\lesssim\; 0.7\,\mu\text{rad} \quad (L_H{}^c = 1.5\,\mu\text{m}, \mathcal{L} = 1\,\text{m}). \tag{3.8}$$

For vertical direction, the angle of β makes the shift at the detector position of $2\mathcal{L}\beta\sin\theta$ when one mirror is out of the vertical (figure 3.4 (2V)) , we get the same requirement as the horizontal case,

$$2\mathcal{L}\beta\sin\theta \;\lesssim\; L_V{}^c \tag{3.9}$$

$$\beta \;\lesssim\; 0.7\,\mu\text{rad} \quad (L_V{}^c = 47\,\text{nm}, \theta = 1\,\text{degree}, \mathcal{L} = 1\,\text{m}). \tag{3.10}$$

In the case of the BSE with the mirror size of s, the wedge angle of $\Delta\theta$ means the parallelism of

$$s\Delta\theta \simeq \lambda_{\text{He-Ne}}/30 \quad (s = 30\,\text{mm}, \lambda_{\text{He-Ne}} = 630\,\text{nm}). \tag{3.11}$$

Parallelism of $\lambda_{\text{He-Ne}}/30$ is required to observe interference fringes. The parallelism of air-spaced etalons reaches $\lambda_{\text{He-Ne}}/150$.

3.3.3 Relative angle

The requirement on the relative angle of $\delta\theta = \theta_2 - \theta_1$ between two BSEs from longitudinal optical path-difference is

$$2D(\sin\theta_2 - \sin\theta_1) \simeq 2D\delta\theta \lesssim L_L{}^c \tag{3.12}$$

$$\delta\theta \lesssim 0.85\,\mathrm{mrad} \simeq 0.05\,\mathrm{degree} \quad (L_L{}^c = 17\,\mathrm{nm}, D = 10\,\mu\mathrm{m}) \tag{3.13}$$

We must arrange two BSEs within the relative angle of 0.05 degree to observe interference fringes with high contrast. The precision of rotating stage is better than 0.002 degree. There is the transverse shift between the superposed two beams of $2D\cos(\theta_1 - \cos\theta_2)$ for horizontal direction at the same time (figure 3.4 (3)), we obtain

$$2D(\cos\theta_1 - \cos\theta_2) \simeq 2D\theta\,\delta\theta \quad \lesssim \quad L_H{}^c. \tag{3.14}$$

At $\delta\theta = 0.05$ degree, the horizontal shift of $2D\theta\delta\theta$ is 0.30 nm which is much smaller than $L_H{}^c$ of $1.5\,\mu$m. The loss of contrast because of the horizontal shift is negligible.

3.3.4 Tilting angle

The tilting angle of α between the two BSEs caused by twisting the optical system makes the vertical shift between the superposed two beams of $2D\sin\alpha$ (figure 3.4 (4)). The requirement as the shift is less than the coherence length is written as

$$2D\sin\alpha \quad \lesssim \quad L_V{}^c \tag{3.15}$$

$$\alpha \quad \lesssim \quad 2.4\,\mathrm{mrad} \simeq 0.13\,\mathrm{degree} \quad (L_V{}^c = 47\,\mathrm{nm}, D = 10\,\mu\mathrm{m}). \tag{3.16}$$

We must adjust two BSEs within the tilting angle of 0.13 degree to observe interference fringes with high contrast. Stages can control tilting angle within this requirement easily.

Tilting of BSE, which can provides the spatial shift with no dispersion, has been utilized for the coherence measurements shown in section 5.5.

3.3.5 Others

Local displacement and slope in one mirror make the distortion of wave front and decrease the contrast of interference fringes by smearing phase of interferogram. Vibration of optical system also cause the smearing in measurement time. Requirements of them are same as described above.

Today's techniques provides us the substrates with the surface roughness of less than a few angstrom. The parallelism of assembled air-spaced etalons reaches to $\lambda_{\mathrm{He\text{-}Ne}}/150$. By using standard stages with the precision of $1/500$ degree for alignment of the BSEs, we can construct Jamin-type interferometer and observe interference fringes with high contrast. The assembly of the two plates into one component is easing the conditions for alignment of the interferometer.

Chapter 4

Facilities

Multilayer fabrication system in KURRI was utilized for making of neutron multilayer mirrors in the interferometer shown in this thesis. All of our experiments using neutrons were performed at cold neutron beam line C3-1-2 "MINE2" at the JRR-3M reactor in JAERI. The beam have a wavelength of 0.88 nm and a bandwidth of 2.7% in full width at half maximum. The details of the optical bench for polarized neutron experiments at MINE2 are also described.

4.1 Multilayer fabrication system

All mirrors which compose interferometers described in this thesis were made by the multilayer fabrication system at KURRI [29]. Vacuum evaporation method is adopted for making the multilayers. The vacuum evaporation system is a modified version of ULVAC MH-60. The vacuum chamber is cylindrical with a 100 cm diameter and 60 cm height. Deposition is done under the pressure of about 1×10^{-5} Torr. During the evaporation
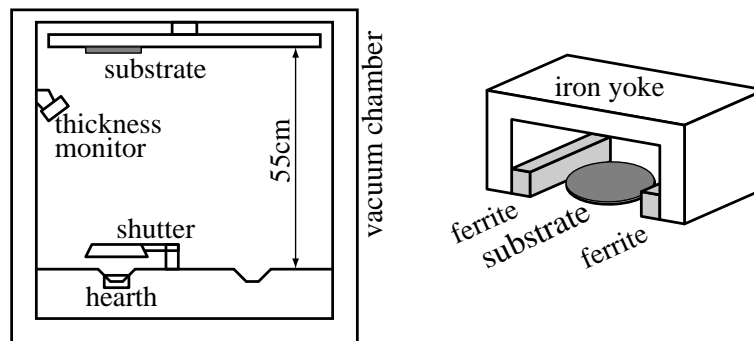
Figure 4.1: Multilayer fabrication system. (Left) Vacuum chamber. (Right) Magnet holder around the substrates. Magnetic field is applied for fabrication of magnetic mirrors.
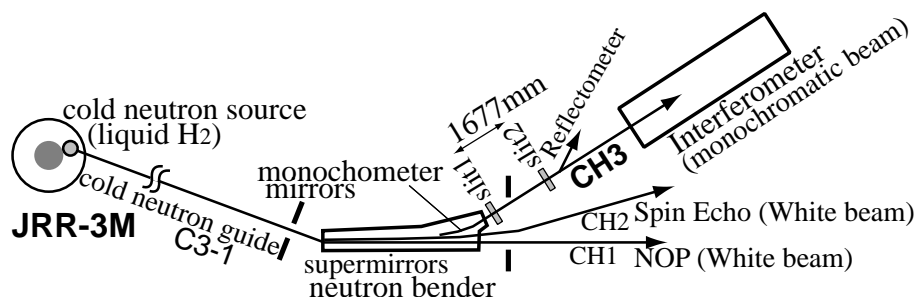
Figure 4.2: Cold neutron beam line MINE2.

of Ni/Ti multilayer air is introduced in order to prevent crystallization, which makes rough surfaces reducing the reflectivity. There are two electric guns for heating samples at the bottom of the chamber. These guns can be used simultaneously. Each gun has four hearths, which are selected remotely. Distance between the hearth and substrates is about 60 cm. A quartz-crystal thickness monitor (ULVAC CRTM) is set on the side wall of the vacuum chamber and the signal from the monitor is inputed to a computer. The shutter, the hearth selector, and the electron gun are controlled automatically by the computer for making the multilayers to specification. In order to make magnetic mirrors magnetic field around the substrates is applied with ferrite (figure 4.1).

The reflectivity of fabricated multilayer is neutron reflectometer at KURRI and JAERI. The parameters for the thickness control system are adjusted to fit the result of neutron reflectivity measurement.

4.2   Cold neutron beam line MINE2

All of our experiments using neutrons were performed at cold neutron beam line C3-1-2 "MINE2" at the JRR-3M reactor in JAERI.

JRR-3M is a pool type research reactor using low enriched aluminide fuels with maximum output of 20MW. Cooling and moderation are done by light water circulation. Beam experimental facilities using horizontal experimental holes are furnished to heavy water tank. Horizontal experimental holes are tangentially set to the reactor core so that only thermal neutron is extracted. For neutron beam experiments, the experimental building "guide hall" is located contiguous to the reactor building. Cold neutrons can be utilized in addition to thermal neutrons for the guide hall. The facility is designed to make thermal neutron penetrate in the liquid hydrogen with 20K, and thereby become cold neutron with lowered speed. Neutrons are guided to the guide hall from the reactor by the neutron guide tubes which are made by rectangular glass tubes covered with vaporized natural nickel film. The size of neutron guide tubes are 200 mm in height and 20 mm in width for thermal neutron, and 120 mm in height and 20 mm in width for cold neutron. Curved tubes supply cold neutrons which are reflected by the insides of the tubes and reduce fast neutrons and gamma ray which become background at experimental hall.
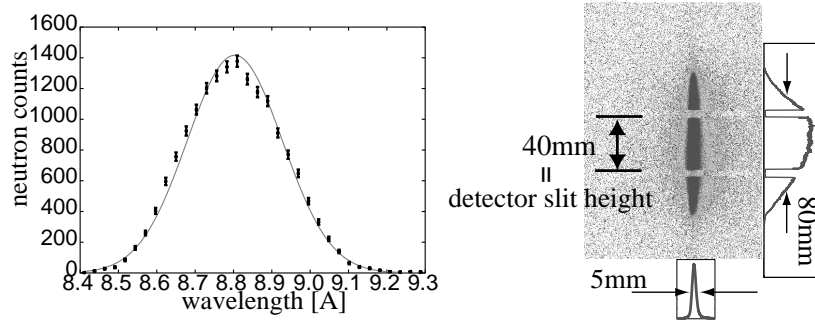
Figure 4.3: (Left) Neutron wavelength measured by time of flight method. The width of the distribution includes uncertainty due to the width of neutron burst. (Right) Image of cross section of neutron beam measured by the imaging plate method at the position about 60cm after beam exit.

The cold neutron guide tube C3 is divided into C3-1 and C3-2 vertically. The size of C3-1 is 50 mm in height and 20mm in width. Neutrons from C3-1 are devised into two beam port, C3-1-1 and C3-1-2.

The supermirror neutron bender is located at beam port C3-1-2 (figure 4.2). The bender with three beam channels using sequential garland reflections supplies neutrons into two white neutron beam lines (CH1 and CH2) and one monochromatic beam line (CH3). The monochromatic beam line, called "MINE2", is for interferometry and reflectometry [30]. The monochromatic neutrons are supplied by reflections of three Ni/Ti multilayer mirrors in the bender. The beam have a wavelength of 0.88 nm and a bandwidth of 2.7% in full width at half maximum. Figure 4.3 shows the wavelength distribution measured by time of flight method with a small disk chopper, which have the effective burst time of 128 μsec. The detector was located at 2977mm after the chopper. The size of the monochromatic beam is 40 mm in height and 5 mm in width. Intensity of MINE2 is about 3000 count per second at the beam divergence of 1/1000 rad and the width of 1 mm.

The neutron beam comes to experimental table through two slits. One is just after exit of the bender and the other is after an aluminum flight tube. The distance between the two slits is 1677 mm. The experimental table is suitable for neutron spin interferometry. Vertical magnetic field of guiding coil keeps polarity of incident neutrons. Magnetic mirrors made with Permalloy45 and germanium are used for a polarizer and an analyzer, and they can be magnetized easily by weak field of the guiding coil. Optical components are on automatic and manual stages (Sigma Koki). The automatic stages are driven by pulsed motors and controlled by a computer. The current of coils for magnetic components are also controlled by the computer. ^{3}He single wire neutron detector is used for counting. The detection efficiency is 100% in the counting rate in our experiment. The signal is analyzed through a preamplifier, an amplifier, an timing single channel analyzer, and an counter (ORTEC). Gamma-ray background is not counted because of pulse height analyzing. The detector is also set on the automatic stages to move the position and swing the window
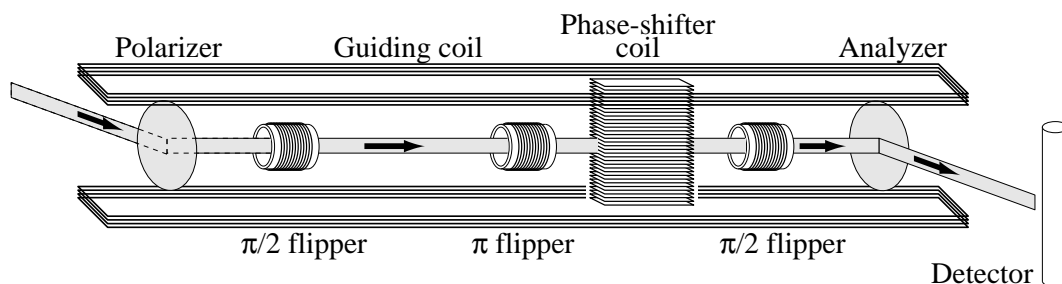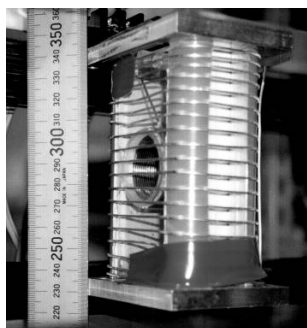
Figure 4.4: Optical devices for spin interferometer.

Figure 4.5: π flipper. Vertical coil around center flipper coil provides weak field for fine correction of resonance condition to guiding field.

for neutron beam. Data is automatically collected by the computer, which controls the stages. Measurements which some parameters of the stages and the coils change in are performed automatically in this system.

4.3   Optical devices for spin interferometry

Neutron optical devices are arranged on the experimental table variously. Neutron spin interferometer with RF flippers can be constructed by placing optical devices on the bench (figure 4.4, see also figure 5.4 in section 5.2). Here the devices which are utilized in the experiments described in this thesis are introduced. The guiding coil consists with a pair of race track type coils with 1.6 m long. The guiding field of about 1 mT is applied. A polarizer and an analyzer are made of magnetic mirrors, which are multilayer mirrors of Permalloy45 and germanium deposited on silicon wafers with diameter of 3 inch. The multilayer mirrors which have the lattice constant of about 15 nm and 40 bilayers are utilized. Mirrors are arranged in an order from the upstream (procedure shown in figure 4.6 (1)(2)(3)). The incident angle of the mirror is determined by scanning for the reflected neutrons, which come to the direction with twice of the incident angle. RF flippers are cylindrical coil with a 30 mm diameter and 30 mm long, which are driven by function generator and amplifiers. The condition of the flippers which gives minimum counts of neutrons through the polarizer, the flipper, and the analyzer is searched by scanning of the frequency and the amplitude. Half of the amplitude is applied for the condition of
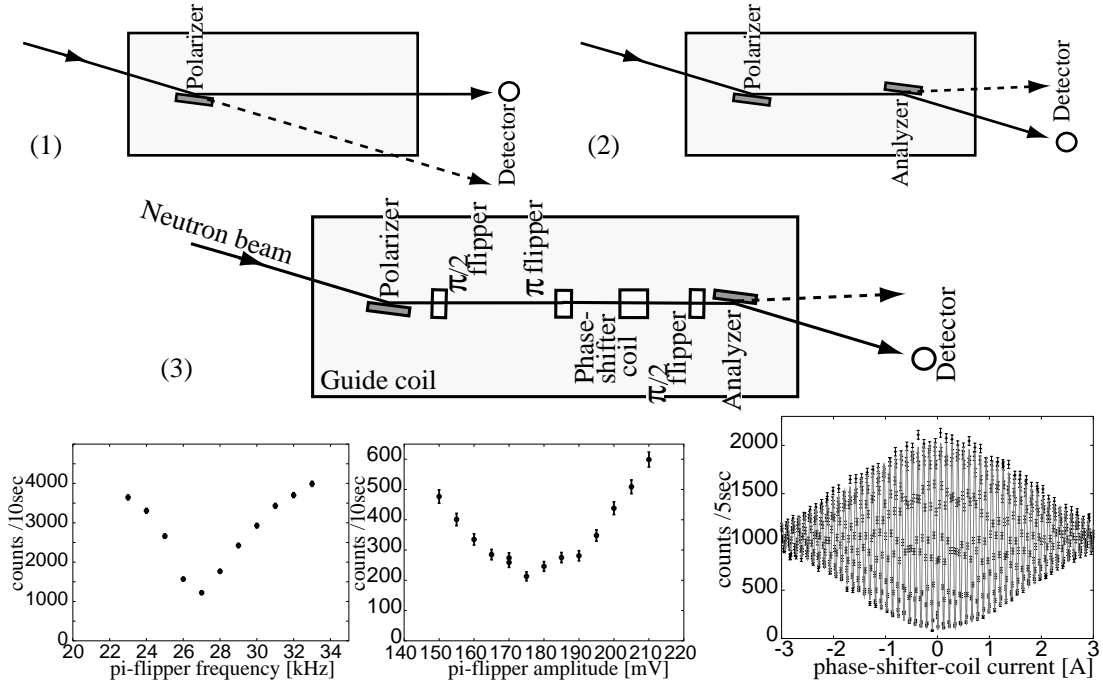
Figure 4.6: Neutron Spin interferometer setup. (Top) Polarizer and analyzer are arranged in an order from the upstream by scanning reflected neutrons. (Middle) Total setup with inserting flippers and phase-shifter coil. (Bottom) Scan of conditions of the RF flipper. First the frequency which gives the minimum count is searched at fixed amplitude (Left). After then the amplitude is scanned at the frequency (Center). In this case 26.9 kHz and 176 mV were applied for following measurements. (Right) Interference fringes by scanning of phase-shifter-coil current.

$\pi/2$ flipper. Interference fringes are observed by scanning of phase-shifter-coil current. We can use various coils as phase-shifters for spin interferometer. Figure 4.6 shows typical fringes by using the phase-shifter-coil with 14 cm long and 240 turns in 20 cm height. The contrast of interference fringes decreases with the current due to the wavelength distribution, according to the equation (2.14). The width of the decrease is consistent with the coherence length determined by the wavelength bandwidth of 2.7% . The contrast achieves to about 92% with the spin interferometer without spinsplitters. The loss of contrast from 100% depends on the performances of the optical components; the guiding field, the polarizer, the analyzer, the flippers, and the phase-shifter coil.

Chapter 5

Jamin-type interferometer using BSEs

Jamin-type interferometer using a pair of BSEs has been demonstrated. We have observed interference fringes with a contrast of 60%. This is the first success of cold-neutron interferometer using four independent multilayer mirrors. The behaviors of phase-shift and echo-point-shit mentioned in chapter 2 has been observed. We have also measured the transverse coherence length of the beam with no dispersion by using our interferometer. These results provide clear understanding of the geometry of Jamin-type arrangement of the BSEs.

5.1 BSEs for spin interferometer

We have prepared a pair of beam splitting etalons with magnetic mirrors. The BSEs function as spinsplitters with large gaps in neutron spin interferometer.

The etalon made of fused silica has a spacing of 9.75μm and has a diameter of 42mm. The mirrors were deposited in a diameter of 20mm on clear aperture of 30mm diameter. The RMS roughness of the present etalon plate is less than 3Å(SLS Optics). The parallelism of the etalon is provided with the matched-front-surfaces of $\lambda_{\text{He-Ne}}/150$ in the
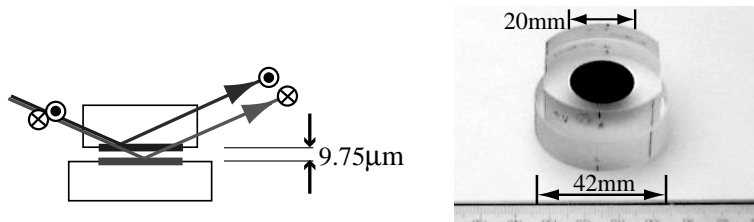
Figure 5.1: Beam splitting etalon with the gap of 10μm.

	Material	Thickness	Bilayer
Magnetic mirror	Permalloy45	154.8Å	8
	Ge	108.4Å	
Non-magnetic mirror	Ni	133.5Å	8
	Ti	98.3Å	

Table 5.1: Materials and thicknesses of multilayer mirrors. Thicknesses are the inputed values for the evaporation system.

specification. The spacers which are polished at the same time has the equal thickness. The mirrors were fabricated by vacuum evaporation method at KURRI (see section 4.1). The magnetic mirror has eight bilayers made of Permalloy45 ($Fe_{55}Ni_{45}$) and germanium. The non-magnetic mirror also has eight bilayers made of nickel and titanium (table 5.1). Results of reflectivity measurements of each mirrors on the etalons is shown in figure 5.3. The etalons function as spinsplitters at the incident angle of 1.05 degree.

5.2   Interference fringes

Our experimental setup for Jamin-type interferometer is shown in figure 5.2. It contains a pair of the BSEs described in the previous section. The distance between the two BSEs was 340mm. The incident angle of the BSEs was 1.05 degree. The angle was controlled by automatic stage (Sigma Koki Model KSH-80PM). The precision of rotating is 1/500 degree. The tilting angle of the BSEs were adjusted by monitoring of reflection of alignment laser (TOPCON Model RL-VH3A). The laser beam keeps level automatically within the precision of 0.003 degree.

In neutron interferometry this is similar to neutron spin interferometer using spinsplitters. The polarizer and $\pi/2$ flipper provide the superposition of spin-up and spin-down component. The first BSE separates up and down spin components into two parallel paths spatially. The waves are superposed each other spatially on the second BSE. Magnetic field
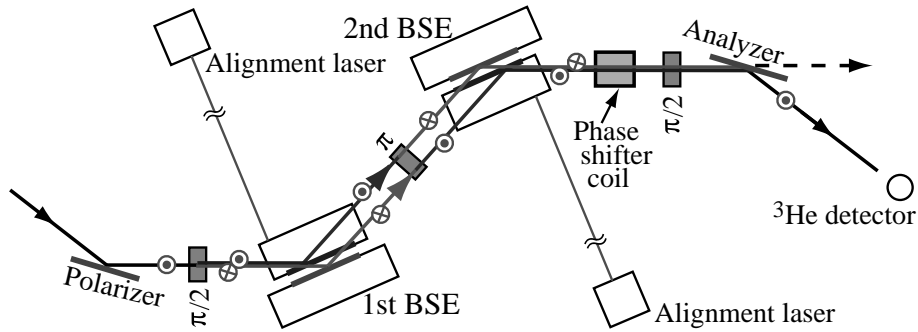
Figure 5.2: Experimental setup.

Potentials for simulation [neV]	
Permalloy45	
up-spin	297.4
down-spin	104.4
Ge	94.1
Ni	243.4
Ti	0.0
SiO_2	90.9
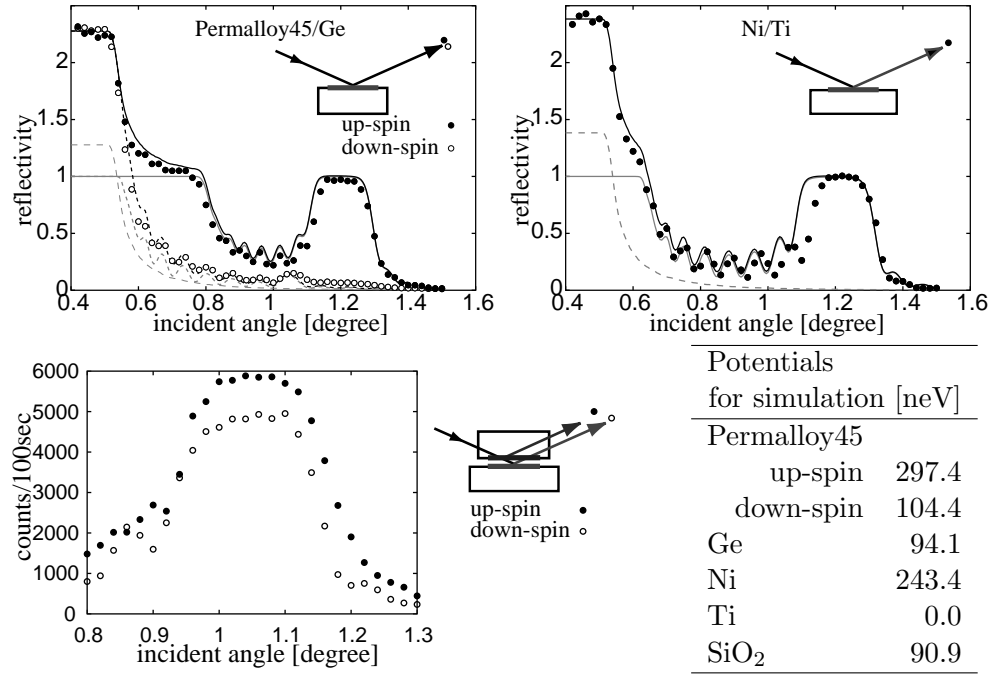
Figure 5.3: (Top) Reflectivity of multilayer mirrors. Dots are results of θ-2θ measurements. Because the mirrors were deposited on the limited area on the substrate, neutrons reflected by uncoated area of the substrate were also counted. The reflectivity in the present charts is normalized by the size of each mirror to adjust the counts in the total reflection range, 0.4–0.5degree, to the reflectivity corresponding to the size of area. Lines show the results of computer simulation. Dashed gray line shows the reflectivity of the uncoated substrate. Solid and dotted gray line shows the reflectivity of the mirror for up-spin and down-spin respectively. Black line shows the sum of the reflectivity of the substrate and the mirror. Solid one and dotted one represents the reflectivity for up-spin and down-spin respectively. Potentials of materials for the simulation are shown in right bottom table. For simulations, thickness of each layer is multiplied by (1/0.93) for solid angle correction because the substrate holder in vacuum evaporation was nearer than normal silicon wafer's case. (Bottom) Reflection measurements of the assembled etalon. The angle which gives peak of counts shifts because of the refraction of the substrate. The loss of counts for down-spin neutrons would be due to the double transmission through the magnetic mirror. The intensity of the two paths is compensated with the reflection off the second BSE, which is arranged in Jamin-type geometry.

Figure 5.4: Experimental setup. Neutron beam come from right side of the pictures.
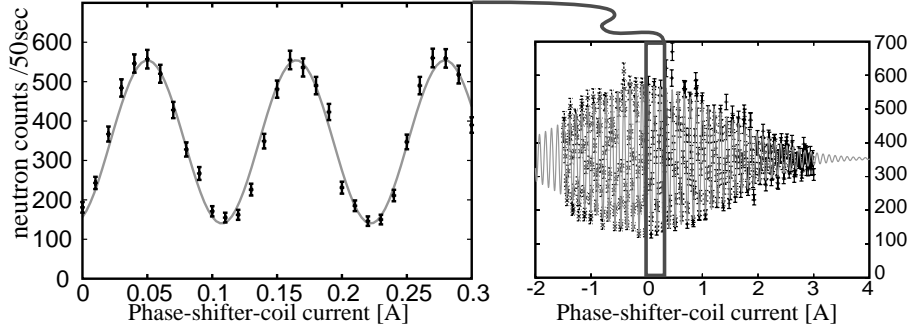
Figure 5.5: Interference fringes by scanning of phase-shifter-coil current. Lines show the fit to the data with coherence function.

provided by the phase-shifter coil gives the relative phase between the two components. By scanning of phase-shifter-coil current interference fringes are observed through the $\pi/2$ flipper and the analyzer mirror. Background counts is about 0.05 counts per second.

We have observed interference fringes with a contrast of $(60\pm2)\%$ by scanning of phase-shifter-coil current (figure 5.5). In the present measurements irregular drift of phase about 0.01rad/min was found, which might be owing to rigidity of the present prototype. This drift is taken into account as systematic error in following discussion, but it doesn't affect our conclusion. Modified version of the interferometer for the rigidity is presented in section 5.6.

5.3 Shiftless component

We observed shiftless component of interferogram with a single reflection off BSE. The fringes by shiftless component had the contrast of 6.4% (figure 5.6). By using equation (2.32), we can estimate that the fringes by shiftless component have the contrast of only 0.4% in the observed fringes with two BSEs. Though figure 5.3 shows the reflectivity
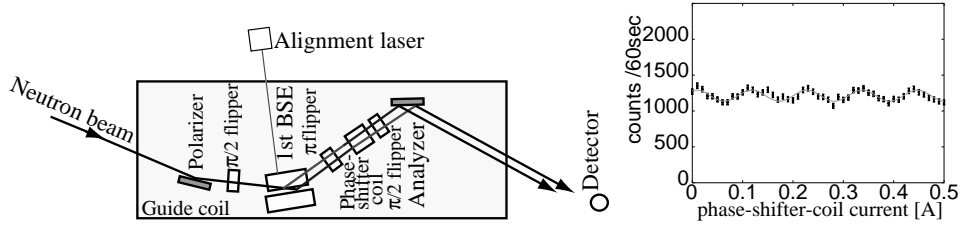
Figure 5.6: (Left) Setup of interferometer with one BSE. (Right) Fringes from shiftless component.
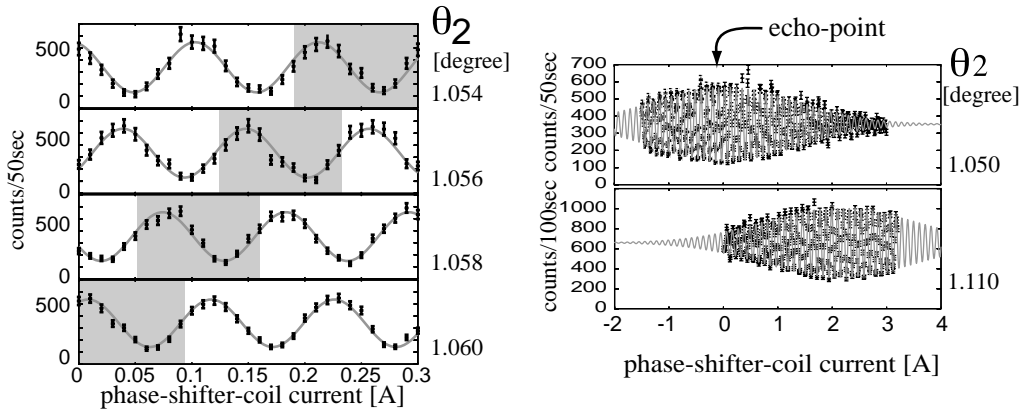
Figure 5.7: (Left) Phase-shift of interference fringes by changing of the second incident angle. (Right) Shift of echo-point.

for spin-down component of the magnetic mirror remain a few percent, the reflectivity of assembled BSE through the etalon substrate is estimated at about 0.5% by simulation using the parameters shown in the figure. This leads the contrast of fringes with one BSE of 7% , which is consistent with the experimental result. The performance of the magnetic mirror is good enough to apply equation (2.32). The small contrast by shiftless component doesn't affect the discussion about phase-shift described below.

5.4 Phase-shift and echo-point-shift

We measured phase-shift of interferogram when the relative angle between the two BSEs changed (left side of figure 5.7). The reflectivity of the mirrors on the etalon remains high in our narrow scanning range. The horizontal shift of the two beam caused by the relative angle of 0.06 degree is 0.4 nm, which is much smaller than the coherence length $L_H{}^c$, therefore the loss of contrast by the transverse shift of the beams is negligible. The echo-point-shift was also observed to the reverse direction of the phase-shift of interferogram (right side of figure 5.7). Through the changes of θ_2 from 1.050degree to 1.060degree a

phase of interferogram was found shifting as

$$-\frac{A_{\mathrm{SS}}k_0}{2\pi}\Delta\theta \quad = \quad -(1.94 \pm 0.04) \times 10^4 \Delta\theta. \tag{5.1}$$

From the right side of figure 5.7 the echo-point shift was evaluated as

$$+\frac{A_{\mathrm{SS}}k_0}{2\pi}\Delta\theta \quad = \quad +(1.93 \pm 0.04) \times 10^4 \Delta\theta. \tag{5.2}$$

The expected value of $\dfrac{A_{\mathrm{SS}}k_0}{2\pi} = \dfrac{2D}{\lambda_0}$ is 2.17×10^4. This discrepancy is understood by the refraction of the etalon substrate of BSE through which the neutrons are transmitted. When we make correction for the refraction by multiplying equation (2.33) by $\dfrac{\sin\theta_2}{\sqrt{(1 - n^2) + \sin^2\theta_2}} = 0.89$, the correcting value of the coefficient $\dfrac{A_{\mathrm{SS}}k_0}{2\pi}$ becomes 1.94×10^4, where n of $(1 - 0.43 \times 10^{-4})$ is the refractive index of the etalon substrate.

5.5 Transverse coherence length

The transverse coherence length can be measured directly by using our new interferometer with BSEs. The interferometer can control the spatial beam shift without dispersion. By twisting this optical system, which is caused by the tilting of the BSE, the interferometer can control the vertical shift between the superposed two waves continuously (figure 5.8). The tilting angle of the second BSE of α makes the vertical shift of $L_V = 2D\sin\alpha$, where D is a spacing of the BSE. We have changed the tilting angle to control the vertical shift
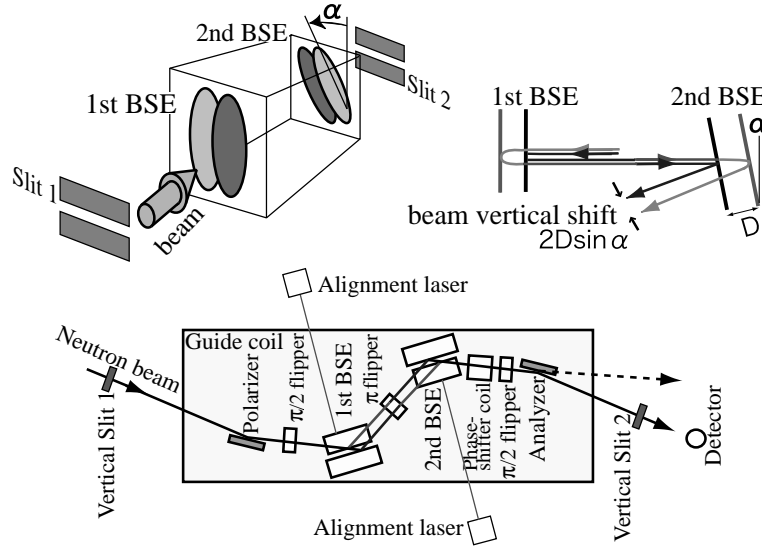
Figure 5.8: (Top) Tilting of the second BSE. Tilting angle makes transverse shift between superposed two beams. (Bottom) Experimental setup for coherence measurements.
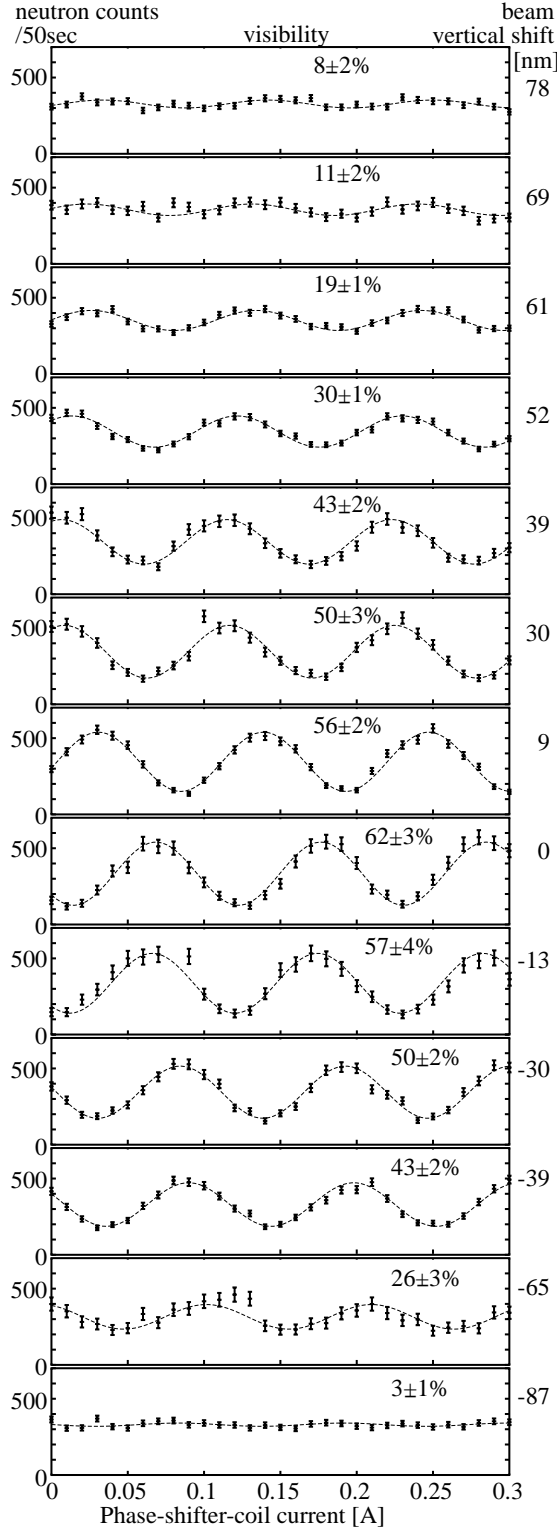
Figure 5.9: Series of interference fringes resulting from scan of phase-shifter-coil current at nearly current for each maximum contrast. The condition of two slits on the beam was the wide one (collimation 1 in Table 5.2). Lines show fit of data.

Table 5.2: Collimation conditions to change the vertical momentum distribution of the neutron beam.

	collimation 1 (wide)	collimation 2 (narrow)
slits width (w) [mm]	40	10
distance (l) [mm]	4855	2675
$\sigma_{k\perp}$ [nm^{-1}]	0.024	0.011
estimate of $L_V{}^c$ [nm]	59	130
measured $L_V{}^c$ [nm]	58±2	129±10
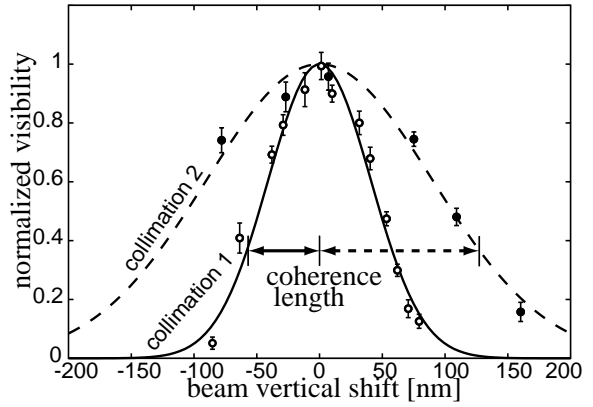
Figure 5.10: Loss of contrast as a function of the vertical shift between superposed two waves. White dots illustrates the observed contrasts in the wide collimation and solid curve is coherence function calculated by equation (2.14). Black dots and dashed curve illustrate those of the narrow collimation. All data are normalized to have a maximum contrast of 1 at $\alpha = 0$. The observed values of maximum contrast were 62±3% and 59±3% for wide collimation and for narrow collimation respectively. The arrows show the coherence lengths which gives the contrast of $1/e$.

and measured a contrast of interference fringes at each situation.

At $\alpha = 0$ we have observed interference fringes with the maximum contrast of 62% by scan of phase-shifter-coil current. In the same scanning range of the phase-shifter-coil current, we have observed the loss of the contrast of interference fringes with the tilting angle of the second BSE (figure 5.9).

The change of the contrast due to the change of neutron glancing angle of the second BSE while the operation of the tilting was small. The glancing angle of the BSE was monitored by the alignment laser in figure 5.8 and the change of the glancing angle was less than 1.1×10^{-4}rad in our measurements. This was able to cause only the change of 1.5% of the observed contrast and this effect is taken into account as systematic error in the following discussion. Irregular drift of phase of interferogram about 0.01rad/min was also found, and this is taken into account as systematic error, too. They don't, however, affect our conclusion.

The vertical momentum distribution of the neutron beam was determined only by two vertical slits on the beam line (Slit 1 and Slit 2 in figure 5.8). The vertical beam collimation was independent from the reflection off the multilayer mirrors as one-dimensional crystals. We changed the width of the slits and the distance between the two slits in order to change the momentum distribution. Table 5.2 shows the two conditions of the slits and the distance. The standard deviation of the vertical wavenumber distribution made by a pair of slits with the width of w and the distance of l is written as

$$\sigma_{k\perp} = \frac{1}{\sqrt{6}} \frac{w}{l} k_0, \tag{5.3}$$

where k_0 is the longitudinal wavenumber of the beam. In this experiment k_0 was 7.14nm^{-1}. We regarded this $\sigma_{k\perp}$ as the standard deviation of Gaussian distribution for equation (2.14) and estimated the coherence length by using equation (2.15).

The measured vertical coherence function of each slit condition is shown in figure 5.10. The contrast decreased with the spatial shift between the superposed two beams. The coherence lengths giving the contrast of $1/e$ was 58±2 nm at the wide collimation. That of the narrow collimation was 129±10 nm. The estimated values by using equation (2.16) are 59nm and 130nm respectively. We have confirmed that the measured coherence length is consistent with the estimate from the coherence function determined by the transverse momentum distribution of the incident beam.

The clear understanding of the three-dimensional coherency depending on the beam collimation and the wavelength dispersion, which are shown in this section and the previous section 5.4, has demonstrated the achievement of precision manipulation for this type of interferometer.

5.6   Stability

Irregular drift of phase about 0.01rad/min was found in the present measurements. Figure 5.11 shows the drift of the phases of fringes by continuous scans without any changing of the setup. The two BSEs were set on two automatic stages individually. The relative
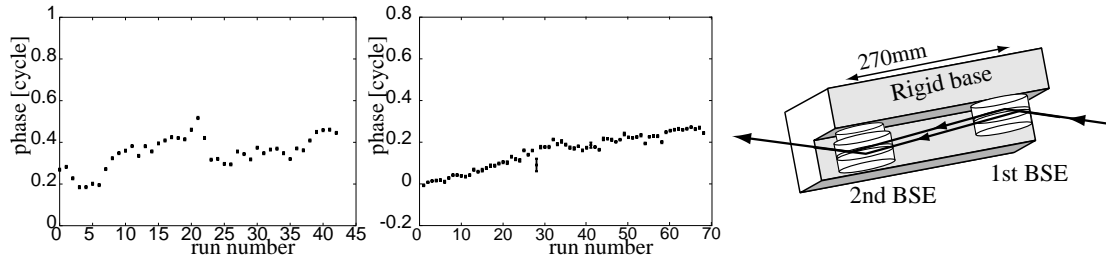
Figure 5.11: (Left) Drift of phase by the original interferometer with two independent BSEs. (about 1 hour/run) (Center) Drift of phase by interferometer with two BSEs on a rigid base. (about 30 min/run) (Right) Rigid base setup. BSEs are pushed onto the surface plane.

angle between the BSEs was not stable because of, for example, vibration of the system, deformation by thermal fluctuation. Surface plane which can hold two BSEs rigidly has been prepared for check the drift reduction. By using the rigid type of interferometer jumping of the drift was reduced, however, the drift was still observed (right hand of figure 5.11). More rigid holding to the surface plane and the stability of the whole of the system are required.

Chapter 6

Discussion

6.1 Contrast of fringes

The maximum of the contrast of observed fringes has reached 62% . Some factors can be considered to the origin of the loss of contrast from 92% , which is the contrast of the interference fringes with the spin interferometer without BSEs in MINE2 (see section 4.3). Here we consider only parallelism between the two mirrors in one BSE for a reason of loss of contrast. The wedge angle $\Delta\theta$ in horizontal direction makes the spatial separation of $L_H = 2\mathcal{L}\Delta\theta$ at detector position, where $\mathcal{L}$ is the distance between BSE and the detector (see section 3.3.2). From equation (2.14) we obtain

$$\exp\left\{-\frac{1}{2}\left(\sigma_{k\perp}L_H\right)^2\right\} \quad \leq \quad \frac{0.62}{0.92} \tag{6.1}$$

$$L_H \quad = \quad 2\mathcal{L}\Delta\theta. \tag{6.2}$$

We find

$$L_H \quad \leq \quad 0.89\,\mu\text{m} \tag{6.3}$$

$$\Delta\theta \quad \leq \quad 0.44\,\mu\text{rad}, \quad (\sigma_{k\perp} = 0.001\,\text{nm}^{-1}, \mathcal{L} = 1\,\text{m}). \tag{6.4}$$

The mirror size s was $(20/\sqrt{2})\,\text{mm}$ in the present case, therefore, the wedge angle corresponds to the parallelism of

$$s\,\Delta\theta \quad \leq \quad 6.3\,\text{nm} \quad = \quad \lambda_{\text{He-Ne}}/100. \tag{6.5}$$

The parallelism between the two mirrors in one BSE must be better than $\lambda_{\text{He-Ne}}/100$, even when the loss of contrast is caused by only the slope of the BSE. This means the good performance of the assembled air-spaced etalons. The good flatness of etalon plates cause no serious distortion of wave front to compose an interferometer. High reflectivity of the multilayer mirrors on the etalon plates show that the surfaces are smooth enough to be used for substrates of neutron mirrors.
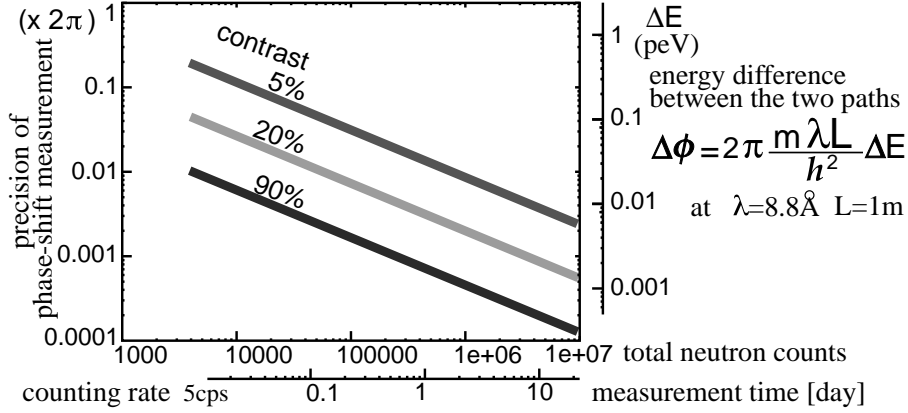
Figure 6.1: Precision of phase-shift measurement for total neutron counts.

6.2   Precision of measurement

Energy difference between the two paths is measured by the phase shift. Here we confirm that the observed energy difference from phase-shift of interferograms is equal to the provided energy difference.

In the present interferometer the observed energy difference ΔE which corresponds to the phase-shift of 2π is

$$\Delta\phi = 2\pi \ = \ 2\pi\frac{m\lambda_n L}{h^2}\Delta E \tag{6.6}$$

$$\Delta E_{\text{observe}} \ \simeq \ \frac{2.4}{L}\,\text{peV} \quad (\lambda_n = 0.88\,\text{nm}), \tag{6.7}$$

The length of the phase-shifter-coil in the present interferometer is $14\,\text{cm}$. We find

$$\Delta E_{\text{observe}} \ \simeq \ 17\,\text{peV} \quad (L = 14\,\text{cm}). \tag{6.8}$$

In the present experiments we provides the energy difference by the magnetic field of phase-shifter coil. The coil has $240\,\text{turn}$ in $20\,\text{cm}$ height. The providing energy difference which corresponds to the cycle of the observed interference fringes of the current of $0.10\,\text{A}$ is

$$\Delta E_{\text{provide}} \ = \ 2\mu B \ \simeq \ 18\,\text{peV}, \tag{6.9}$$

which is equivalent to the observed one. The discrepancy can be understood as an effect from the difference of the interaction length L, for example, the leak field of the coil.

This means that we can measure the energy difference between the two paths of $17\,\text{peV}$ by observation of the phase-shift of 2π. Energy resolution of an interferometer for experiments depends on the precision of phase-shift measurements. That of the present interferometer reaches $1\,\text{peV}$ or better when we can decide the phase of fringes in the order of $0.1\,\text{rad}$. Figure 6.1 shows rough estimate of the precision of phase shift measurement
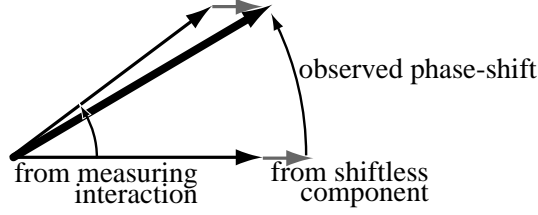
Figure 6.2: Phase-shift by both of shifted fringes and shiftless fringes in Gauss plane. The amplitude and the angle of the vector represents the contrast and the phase of interference fringes respectively.

by computer simulation, which is considered with only statistical error. High contrast of interference fringes is quite important for phase-shift measurements. By using an interferometer which provides the fringes with the contrast of 60% the phase-shift of the order of 1 mrad can be measured for a few days, when the interaction and no-interaction are applied one after the other in a short cycle to trace the drift of phase of interferogram. In the presented interferometer, however, irregular drift of phase has reduced the precision for phase-shift measurements. By using the interferometer with the rigid base shown in section 5.6, the residual of phase of stable consecutive nine runs from linear fit was 0.02 rad, which is a limit in the present state. The stability is also important for high precision measurements. When the interaction length is 1 m and the neutron wavelength is 0.88 nm, the energy resolution reaches to a few femto-electronvolts.

6.3 Phase-shift with shiftless component

We observe the phase-shift as sum of the phase-shift by the searching interactions and the small phase-shift by shiftless component (figure 6.2). When the change of the relative angle between the two phase is $\pi/2$, the difference between the observed phase-shift and the searching phase-shift becomes maximum. In the present case, the maximum difference can amount to

$$\phi_{\text{real}} - \phi_{\text{observed}} \quad \simeq \quad \tan^{-1} \frac{\Upsilon_{\text{Shiftless}}}{\Upsilon_{\text{DoubleSS}}} \simeq \tan^{-1} \frac{0.004}{0.6} \tag{6.10}$$

$$\simeq \quad 0.007 \, \text{rad}, \tag{6.11}$$

which is only 0.4% of the real shift of $\pi/2$. The modification of the coefficients of phase-shift $\frac{A_{\text{SS}} k_0}{2\pi} = (1.94 \pm 0.04) \times 10^4$ described in section 5.4 is not required in the precision of the present experiments.

Though the shiftless component is small enough in this case, the fringes from the shiftless component can prevents us from finding small phase-shift to be searched for. Estimation of shiftless component is quite important for measurements using spin interferometer. We can measure directly the amount of shiftless component of each path in the case of a spin interferometer with perfectly separated paths.

On the other hand, when the two paths are not characterized by spin eigenstates in an interferometer, there is no shiftless component.

As a result of the experiments and the discussions as shown above, we can remark that the present interferometer of Jamin type has demonstrated the feasibility of interferometer using four multilayer mirrors deposited on independent substrates. The parallelism between the two planes in each BSE and the equality of gap spacing of the two BSEs ensure the alignment of the mirrors within the precision required by the three-dimensional coherency of the beam. Some applications with this type of interferometer with large path separation are discussed in the next chapter.

Chapter 7

Applications

Some more applications with the cold-neutron interferometry using BSEs are discussed. Various arrangements of BSEs enables us to build new types of coherent optical systems. We can investigate not only fundamental physics, for example, Aharonov-Chaser effect, but also soft material science and biophysics by neutron spin echo method.

7.1 Aharonov-Casher effect

Aharonov-Casher effect for neutral particles with a magnetic moment is electromagnetic and quantum mechanical dual of the Aharonov-Bohr effect for charged particles (figure 7.1) [31, 32]. The relative phase is introduced when the movement of a magnetic dipole around an electric charge. The AC phase shift is given by

$$\phi_{\mathrm{AC}} = \pm \frac{4\pi\mu\Lambda}{\hbar c} \quad , \quad \Lambda = 2LE/4\pi, \tag{7.1}$$

where Λ is effective lineal charge density, L is interaction path length, and E is electric field between electrodes.
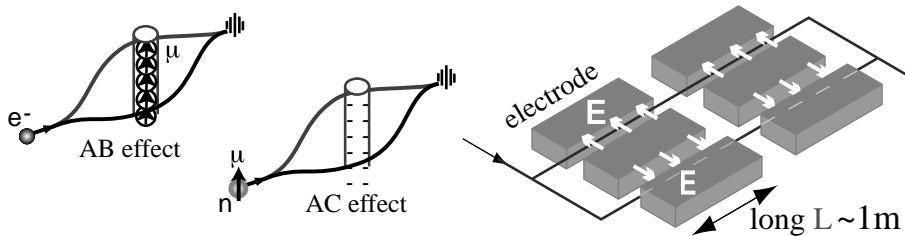
Figure 7.1: Aharonov-Casher effect.
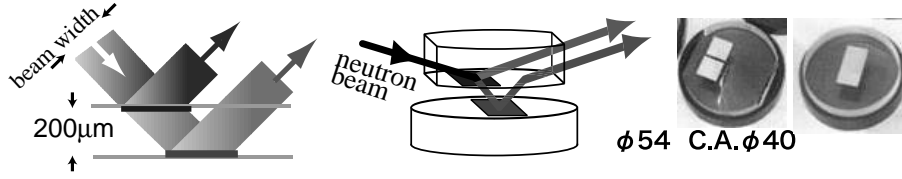
Figure 7.2: BSE with the space-length of 200μm. Multilayer mirrors were deposited in limited area.
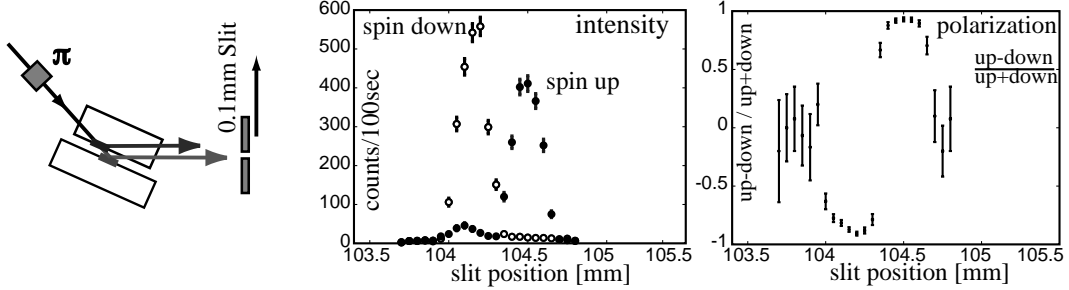
Figure 7.3: Spatial separation by BSE with the space-length of 200μm. (Left) Profile scan for each spin component. (Right) Polarization at each position.

The measurement using silicon perfect crystal neutron interferometer was performed at the University of Missouri Research Reactor [15]. The small interaction path length was 2.53 cm and the expected phase shift was 1.50 mrad. The measured value was 2.19 ± 0.52 mrad and there is a discrepancy. High precision experiments using atom interferometer have been done[33, 34, 35], however, the two paths were not separated spatially and the experiments could not discuss the topological nature of the AC effect[16].

The AC phase-shift is proportional to the interaction length L. Large L in the Jamin-type interferometer using BSEs is capable of high precision measurement. When we use an interferometer with large spatial separation by BSEs, we can manifest the topological nature of AC effect.

We have already prepared new BSEs with the spacing of 200μm . The etalon plates have a diameter of 54 mm and clear aperture of 42 mm diameter. Neutron mirrors were deposited in limited area as shown in figure 7.2. Neutron beam which has proper incident angle can be split into two perfectly separated paths. Two multilayer neutron mirrors in one BSE are same as the two multilayer in the BSE mentioned in section 5.1 Beam profile has been scanned after reflection off the BSE with incident angle of 1.05 degree (figure 7.3). The two beams are separated and corresponds to up- and down-spin component.

We have also prepared the electrodes for AC measurements with long interaction length (figure 7.4). The interaction length L is 20 cm, which is about ten times as long as that of the previous experiment using silicon crystal. When the electric field as strong as the previous case can be applied, the interferometer with the BSEs and these electrodes is ten times as sensitive as the previous silicon's case. The discrepancy of the order of 0.1mrad, which was observed by the silicon's experiments, can be examined by a few day's
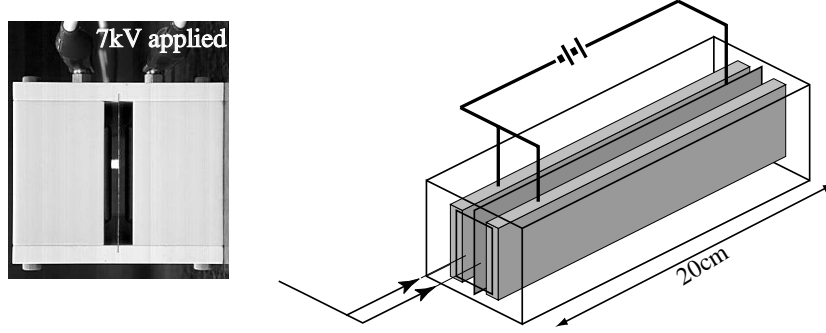
Figure 7.4: Electrode for AC measurements. Photograph on left-hand show spark discharge between electrodes occurred at 7kV applied without special treatments.

experiments (see figure 6.1 in section 6.2). Though the electrodes is not treated specially for spark discharge at present, the present one is even twice as sensitive as the previous one.

7.2 Neutron Spin Echo spectrometer

Neutron spin echo (NSE) is an unique method which measures the energy transition of quasi-elastic scattering by using spin rotation of a neutron [36, 37]. The conventional way to rotate neutron spin is Larmor precession by magnetic field. Neutron spin which is polarized in xy-plane rotate around magnetic field in z-direction (figure 7.5). The neutron polarization losses by the dispersive action of the Larmor rotation in the first field, however, the second magnetic field in reverse direction makes reverse rotation of the neutron and the polarization is compensated. When there is energy transition by scattering by a sample, the rotation number in the second field changes. The compensation of polarization becomes insufficient and the contrast of interference fringes decreases. The energy transition is measured by observing the loss of contrast of the interference fringes.

A BSE using a magnetic mirror, which is regarded as a spinsplitter with the large gap, makes large relative phase between up- and down-spin components. This is equivalent to large spin rotation in xy-plane. (++) arrangement of two BSEs shown in figure 7.6 makes much larger relative phase and superposes spatially the two spin components at sample position. The relative phase is

$$\phi = 4\pi \frac{2D\sin\theta}{\lambda_n},$$

where D is the spacing of the BSEs and θ is the incident angle to the BSE. The (++) arrangement is equivalent to the first magnetic field of the conventional spin echo system. The same arrangement of two BSEs, which is called as (−−) because of the reverse aspect, functions as the second magnetic field to compensates the spin rotation. When the incident angle to the first BSE changes into $\theta + \delta\theta$, the angle to the second BSE changes into $\theta - \delta\theta$.
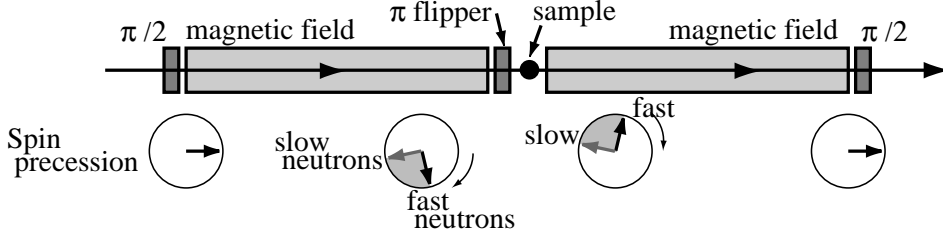
Figure 7.5: Neutron spin echo spectrometer. Usually the second magnetic field has the same direction of the first one and π-flipper is located between the two fields.

The total relative phase is

$$\phi' = 2\pi \frac{2D(\sin(\theta + \delta\theta) + \sin(\theta - \delta\theta)))}{\lambda_n} \tag{7.2}$$

$$\simeq 4\pi \frac{2D \sin\theta \cos\delta\theta}{\lambda_n}, \tag{7.3}$$

which changed only with $\cos\delta\theta$. This means that the $(++)$ arrangement of two BSEs is insensitive to the beam divergence by scattering by the sample.

When the energy transition makes wavelength shift from λ_n to $\lambda_n + \delta\lambda$, the total phase through four BSEs is

$$\phi = 8\pi D \sin\theta \left\{ \frac{1}{\lambda_n} - \frac{1}{\lambda_n + \delta\lambda} \right\} \tag{7.4}$$

$$\simeq \frac{8\pi D \sin\theta}{\lambda_n} \delta\lambda. \tag{7.5}$$

The energy transition is written as

$$\hbar\omega = \frac{h^2}{2m} \left\{ \frac{1}{\lambda_n{}^2} - \frac{1}{(\lambda_n + \delta\lambda)^2} \right\} \tag{7.6}$$

$$\simeq \frac{h^2 \, \delta\lambda}{m\lambda_n{}^3}. \tag{7.7}$$

The fourier time τ, which characterize the performance of spin echo system, is defined as

$$\phi = \omega\tau. \tag{7.8}$$

We find

$$\tau = \frac{4mD\lambda_n \sin\theta}{h}. \tag{7.9}$$

Neutron spin echo spectrometer enables us to study slow dynamics in the order of the fourier time. In BSE's case the fourier time depends on the spacing of BSEs. Long fourier time has the advantage in investigation of soft material science and biophysics, and can
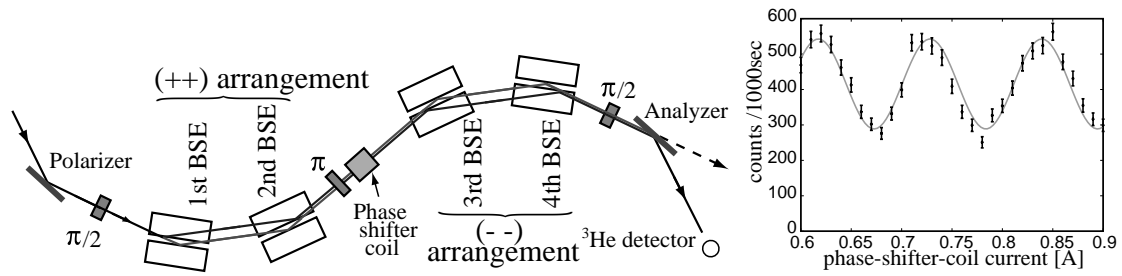
Figure 7.6: Neutron spin echo spectrometer using four BSEs.

be realized by using large-spacing BSEs. Using the BSEs with the gap of 200μm and neutrons of wave-length of 20Å, the fourier time of the spectrometer reaches up to about 300ns.

Test experiments have been performed with four BSEs with spacing of $9.75\,\mu$m. In this case fourier time is 1.5 nsec. We have observed the interference fringes with the contrast of 30% without sample by scanning of phase-shifter-coil current. We are continuing test experiments to study the characters of the spectrometer using BSEs precisely.

7.3 Mach-Zehnder type interferometer

The results reported in this thesis have qualified the flatness and roughness of the present etalon plates as good substrates enough to be used for neutron mirrors, which cause no serious distortion of wave front to compose an interferometer. Arranging such mirrors, now we are capable of establishing even a Mach-Zehnder type interferometer.

Prototype of Mach-Zehnder interferometer for cold neutrons using multilayer mirrors has been prepared. By using a surface plane of about 50 cm long, which has the flatness of $\lambda_{\text{He-Ne}}/20$, four mirrors can be aligned within the precision required by coherency of the beam [39].
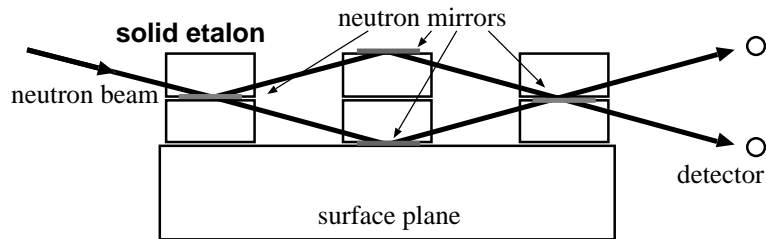
Figure 7.7: Mach-Zehnder type interferometer.

COW experiments

In gravitationally-induced quantum interference experiment, which is called as "COW experiment" [13] the phase shift is given by

$$\phi_g = -2\pi m^2 \frac{g}{h^2} \lambda_n A \sin\theta \qquad\qquad (7.10)$$

where A is the area enclosed by beam path, θ is tilting angle of interferometer. It is reported that there is a discrepancy of 0.8% of phase shift between theory and experiment [14]. Long wavelength neutrons and large area of interferometer enable us to carry out higher precision measurement. The experiments using Bragg reflection off multilayer mirrors needs much smaller correction for dynamical diffraction effects than that of silicon perfect crystal interferometer. Small tilting angle which prevent from bending the interferometer is sufficient for phase shift measurements. Mach-Zehnder interferometer for cold neutrons is suitable for the COW experiment. Our prototype is about ten times as sensitive as the conventional silicon crystal's case because of the large area of the interferometer and long wavelength of neutrons.

Chapter 8

Conclusion

New type of neutron optical component "beam splitting etalon (BSE)" have been developed. Spatial separation between two paths in an interferometer for cold neutrons has enlarged by using BSEs.

Jamin-type interferometer using a pair of BSEs with the spacing of 9.75μm has been demonstrated. This is the first success of cold-neutron interferometer using four multilayer mirrors deposited on independent substrates. The parallelism between the two mirrors in each BSE and the equality of gap thicknesses of the two BSEs ensure the alignment of the four mirrors within the precision required by the three-dimensional coherency of the beam. We have observed interference fringes with a contrast of 60%.

The relative phase between the two paths in the interferometer is provided by both the magnetic field of phase-shifter-coil and by the spacing of BSEs. We have demonstrated clearly the shift of the phase of interferogram and the shift of the echo-point according to coherence function depending on the finite monochromaticity of the beam. We have also observed that the contrast varies according to the coherence function determined by the collimation of the beam and measured the transverse coherence length directory.

The achievement of precision manipulation for this type of interferometer system has been demonstrated by the clear understanding of the three-dimensional coherency depending on the beam collimation and the wavelength dispersion. The flatness and roughness of the present etalon plates have been qualified as good substrates enough to be used for neutron mirrors, which cause no serious distortion of wave front to compose an interferometer.

We have discussed possible applications of this type of interferometer for studying fundamental physics. BSEs with spacing of 200μm thickness have created for measurement of the topological Aharonov-Casher (AC) effect and the perfect spatial separation between the two beams through the BSE has been demonstrated. The interferometer using the BSEs and new electrode, which have ten times long interaction length than conventional one, has the advantage to increase the sensitivity for AC phase shift. New type of spin echo spectrometer can be realized by $(++--)$ arrangement of four BSEs. We have also construct a prototype and performed experiments without samples.

Acknowledgments

References

[1] E. Fermi and W. H. Zinn, Phys. Rev. **70**, 103 (1946).

[2] H. Maier-Leibniz and T. Springer, Z. Phys. **167**, 386 (1962).

[3] C. G. Shull, Phys. Rev. **179**, 752 (1969).

[4] V. F. Sears, *Neutron Optics* (Oxford University Press, Oxford, 1989).

[5] U. Bonse and H. Rauch, *Neutron Interferometer* (Clarendon, Oxford, 1979).

[6] H. Rauch and S. A Werner, *Neutron Interferometry* (Oxford University Press, Oxford, 2000).

[7] S. Yamada, T. Ebisawa, N. Achiwa, T. Akiyoshi,and S. Okamoto, Annu. Rep. Res. Reactor Inst. Kyoto Univ. **11**, 8 (1978).

[8] T. Ebisawa, N. Achiwa, S. Yamasa, T. Akiyoshi, and S. Okamoto, J. Nucl. Sci. Technol. **16**, 647 (1979).

[9] S. Tasaki, J. Appl. Phys. **71**, 2375 (1992).

[10] S. Tasaki, Doctor thesis, Dep. of Nuclear Engineering, Kyoto University **71**, 2375 (1995).

[11] U. Bonse and M. Hart, App. Phys. Lett. **6**, 155 (1965).

[12] H. Rauch, W. Treimer, and U. Bonse, PhysĖettÅ **47**, 369 (1974).

[13] R. Collella, A. W. Overhauser, and S. A. Werner, Phys. Rev. Lett. **34**, 1472 (1975).

[14] K. C. Littrell, B. E. Allman, and S. A. Werner, Phys. Rev. A **56**, 1767 (1997).

[15] A. Cimmino, G. I. Opat, and G. Klein , Phys. Rev. Lett. **63**, 380 (1989).

[16] A. Cimmino, B. E. Allman, A. G. Klein, H. Kaiser, and S. A. Werner, Nucl. Inst. and Meth. A **440**, 579 (2000).

[17] S. A. Werner, R. Colella, A. W. Overhauser, and C. F. Eagen, Phys. Rev. Lett. **35**, 1053 (1975).

[18] H. Rauch, A. Zeilinger, G. Badurek, A. Wilfing, W. Bauspiess, and U. Bonse, Phys. Lett. A **54**, 425 (1975).; H. Rauch, A. Wilfing, W. Bauspiess, and U. Bonse, Z. Phys. **B29**, 281 (1978).

[19] H. Kaiser, S. A. Werner, E. A. George, Phys. Rev. Lett. **50**, 560 (1983).

[20] H. Rauch and H. Wölwitsch, Phys. Rev. A **53**, 902 (1996).

[21] A. I. Ioffe, B. S. Zabiyakin, and G. M. Drabkin, Phys. Lett. **111**, 373 (1985).

[22] M. Gruber, K. Eder, A. Zeilinger, R. Gähler, and A. Mampe, Phys. Lett. A **140**, 363 (1989).

[23] H. Funahashi, T. Ebisawa, T. Haseyama, M. Hino, A. Masaike, Y. Otate, T. Tabaru, and S. Tasaki, Phys. Rev. A **54**, 649 (1996).

[24] T. Ebisawa, S. Tasaki, M. Hino, N. Achiwa, Y. Otake, H. Funahashi, D. Yamazaki, and T. Akiyoshi, Phys. Rev. A **57**, 4720 (1998).

[25] D. Yamazaki, Doctor thesis, Dep. of Nuclear Engineering, Kyoto University , (2002).

[26] Y. Otake, H. Funahashi, S. Tasaki, T. Ebisawa, and T. Kawai, *Proceedings of 6th International Symposium on Foundations of Quantum Mechanics in the Light of New Technology (ISQM-Tokyo '98)*, edited by Y. A. Ono and K. Fujikawa (Elsevier Science, 1999), 323.

[27] T. Kawai, T. Ebisawa, S. Tasaki, M. Hino, D. Yamazaki, A. Akiyoshi, Y. Matsumoto, N. Achiwa, and Y. Otake, Nucl. Inst. and Meth. A **410**, 259 (1998).

[28] Y. Morikawa and Y. Otake, Il Nuovo Cimento **105**, 507 (1990).

[29] S. Tasaki,, Nucl. Inst. and Meth. A **355**, 501 (1995).

[30] T. Ebisawa, S. Tasaki, Y. Otake, H. Funahashi, K. Soyama, N. Torikai, Y. Matushita, Physica B **213 & 214**, 901 (1995).

[31] Y. Aharonov and A. Casher, Phys. Rev. Lett. **53**, 319 (1984).

[32] J. Anandan, Phys. Lett. **138**, 347 (1989).

[33] K. Sangster, E.A. Hinds, S.M. Barnett, E. Riis, and A.G. Sinclair, Phys. Rev. A **51**, 1776 (1995).

[34] A. Grörliz, B. Schuh, and A. Weis, Phys. Rev. A **51**, R4305 (1995).

[35] K. Zeiske, F. Riehe, G. Zinner, and J. Helmcke, App. Phys. B **60**, 205 (1995).

[36] F. Mezei, Z. Phys. **255**, 146 (1972).

[37] F. Mezei, *Lecture Notes in Physics Neutron Spin scho, Vol.128* (Splinger, Berlin, 1980).

[38] T. Ebisawa, D. Yamazaki, S. Tasaki, M. Hino, Y. Iwata, N. Achiwa, T. Kanaya, and K. Soyama, Phys. Lett. A **259**, 20 (1999).

[39] K. Taketani, Master thesis, Dep. of Physics, Kyoto University (2004).